The Astrophysical Journal, 880:37 (20pp), 2019 July 20 https://doi.org/10.3847/1538-4357/ab287a

Relativistic Magnetic Reconnection in Electron–Positron–Proton Plasmas: Implications for Jets of Active Galactic Nuclei

Maria Petropoulou[1], Lorenzo Sironi[2], Anatoly Spitkovsky[1], and Dimitrios Giannios[3,4,5]
[1] Department of Astrophysical Sciences, Princeton University, 4 Ivy Lane, Princeton, NJ 08544, USA; m.petropoulou@astro.princeton.edu
[2] Department of Astronomy, Columbia University, 550 W 120th Street, New York, NY 10027, USA
[3] Department of Physics & Astronomy, Purdue University, 525 Northwestern Avenue, West Lafayette, IN 47907, USA
[4] Department of Physics, University of Crete, Voutes, GR-70013, Heraklion, Greece
[5] Institute of Astrophysics, Foundation for Research and Technology Hellas, Voutes, GR-70013, Heraklion, Greece
Received 2019 April 13; revised 2019 May 24; accepted 2019 June 6; published 2019 July 23

Abstract

Magnetic reconnection is often invoked to explain the nonthermal radiation of relativistic outflows, including jets of active galactic nuclei (AGNs). Motivated by the largely unknown plasma composition of AGN jets, we study reconnection in the unexplored regime of electron–positron–proton (pair-proton) plasmas with large-scale two-dimensional particle-in-cell simulations. We cover a wide range of pair multiplicities (lepton-to-proton number ratio $\kappa = 1$–199) for different values of the all-species plasma magnetization ($\sigma = 1$, 3, and 10) and electron temperature ($\Theta_e \equiv kT_e/m_e c^2 = 0.1$–100). We focus on the dependence of the post-reconnection energy partition and lepton energy spectra on the hot pair plasma magnetization $\sigma_{e,h}$ (i.e., the ratio of magnetic to pair enthalpy densities). We find that the post-reconnection energy is shared roughly equally between magnetic fields, pairs, and protons for $\sigma_{e,h} \gtrsim 3$. We empirically find that the mean lepton Lorentz factor in the post-reconnection region depends on σ, Θ_e, and $\sigma_{e,h}$ as $\langle \gamma_e - 1 \rangle \approx \sqrt{\sigma}(1 + 4\Theta_e)(1 + \sigma_{e,h}/30)$, for $\sigma \geqslant 1$. The high-energy part of the post-reconnection lepton energy distributions can be described by a power law, whose slope is mainly controlled by $\sigma_{e,h}$ for $\kappa \gtrsim 3$–6, with harder power laws obtained for higher magnetizations. We finally show that reconnection in pair-proton plasmas with multiplicities $\kappa \sim 1$–20, magnetizations $\sigma \sim 1$–10, and temperatures $\Theta_e \sim 1$–10 results in particle power-law slopes and average electron Lorentz factors that are consistent with those inferred in leptonic models of AGN jet emission.

Key words: acceleration of particles – galaxies: active – magnetic reconnection – plasmas

1. Introduction

A fundamental question in the physics of astrophysical relativistic outflows is how their energy, which is initially carried in the form of Poynting flux, is first transferred to the plasma and then radiated away to power the observed emission. Magnetic field dissipation via reconnection has been often invoked to explain the nonthermal signatures of pulsar wind nebulae (PWNe; e.g., Lyubarsky & Kirk 2001; Pétri & Lyubarsky 2007; Sironi & Spitkovsky 2011a; Cerutti et al. 2012; Philippov & Spitkovsky 2014; see Sironi & Cerutti 2017 for a recent review), gamma-ray bursts (GRBs; e.g., Thompson 1994; Usov 1994; Spruit et al. 2001; Drenkhahn & Spruit 2002; Lyutikov & Blandford 2003; Giannios 2008; Beniamini & Giannios 2017), and jets from active galactic nuclei (AGNs; e.g., Romanova & Lovelace 1992; Giannios et al. 2009, 2010; Giannios 2013; Petropoulou et al. 2016; Nalewajko et al. 2018; Christie et al. 2019).

In most relativistic astrophysical outflows, reconnection proceeds in the so-called relativistic regime in which the Alfvén velocity of the plasma approaches the speed of light (or equivalently, the plasma magnetization, defined as the ratio of magnetic to particle enthalpy densities, is $\sigma \gtrsim 1$). The physics of reconnection can only be captured from first principles by means of fully kinetic particle-in-cell (PIC) simulations. Extensive numerical work on relativistic reconnection of electron–positron (pair) plasmas has been performed in two dimensions (e.g., Zenitani & Hoshino 2001, 2007; Daughton & Karimabadi 2007; Cerutti et al. 2012; Sironi & Spitkovsky 2014; Guo et al. 2014, 2015; Liu et al. 2015; Nalewajko et al. 2015; Sironi et al. 2015, 2016; Werner et al. 2016; Hakobyan et al. 2019; Kagan et al. 2018; Petropoulou & Sironi 2018) and in three dimensions (e.g., Zenitani & Hoshino 2005, 2008; Liu et al. 2011; Sironi & Spitkovsky 2011a, 2012; Kagan et al. 2013; Cerutti et al. 2014; Sironi & Spitkovsky 2014; Guo et al. 2015; Werner & Uzdensky 2017), whereas the study of transrelativistic and relativistic reconnection in two-dimensional electron–proton plasmas became possible more recently (e.g., Melzani et al. 2014; Sironi et al. 2015; Guo et al. 2016; Rowan et al. 2017; Ball et al. 2018; Werner et al. 2018).

In contrast to other astrophysical outflows, such as PWNe, the plasma composition of astrophysical jets is largely unknown. On the one hand, there is no direct way of probing the plasma composition in jets, and on the other hand, there are large theoretical uncertainties about the jet baryon loading mechanisms (for recent kinetic simulations of black hole jet launching, see Parfrey et al. (2019)). As a result, any attempts to infer the jet plasma composition rely on the modeling of the emitted radiation (e.g., Ghisellini 2012; Ghisellini et al. 2014), which, however, suffers from degeneracies that are inherent in the radiative models. For AGN jets, in particular, both pair and electron–proton compositions have been discussed in the literature. A pure pair composition in powerful AGN jets (e.g., in flat spectrum radio quasars; henceforth FSRQs) is disfavored because bulk Comptonization of the ambient low-energy photons by the pairs would result in luminous spectral features in X-rays that are not observed (e.g., Sikora et al. 1997; Sikora & Madejski 2000; cf., Kammoun et al. 2018). This argument does not apply to less powerful jets (such as BL Lac type sources), because the ambient radiation fields are weak or even absent, and a pure pair plasma cannot be excluded in this case. If jets are devoid of pairs, i.e., they are composed of electron–proton plasmas, the inferred power

(which is dominated by the kinetic power of protons) is large, usually exceeding the accretion power (e.g., Ghisellini et al. 2014; Madejski et al. 2016). A mixed composition with tens of pairs per proton may be more realistic, as it can reduce the inferred jet power by a factor equal to the lepton-to-proton number ratio; the so-called pair multiplicity (e.g., Ghisellini et al. 2010; Ghisellini 2012; Madejski et al. 2016). The presence of pairs in the dissipation regions of jets is also expected to affect the average energy per lepton available for particle heating, as well as the efficiency with which nonthermal particles are accelerated.

The goal of this work is to study the general properties of relativistic reconnection in the unexplored regime of plasmas with mixed composition. We focus on electron–positron–proton (or pair-proton) plasmas, as they bridge the gap between the pair plasma and electron–proton plasma cases that have been extensively studied in the past. We perform a suite of large-scale 2D PIC simulations using the realistic proton-to-electron mass ratio ($m_i/m_e = 1836$) while varying three physical parameters, namely the plasma magnetization ($\sigma = 1$, 3, and 10), the plasma temperature ($\Theta_e \equiv kT_e/m_e c^2 = 0.1 - 100$ with equal electron and proton temperatures), and the number of pairs per proton ($\kappa = 1$–199). In this study, even in cases where the pairs dominate by number, the plasma rest-mass energy is governed by protons. We study, for the first time, the inflows and outflows of plasma in the reconnection region, the energy partition between pairs, protons, and magnetic fields, and the energy distributions of accelerated particles as a function of the pair multiplicity.

This paper is organized as follows. In Section 2, we describe the setup of our simulations. In Section 3, we present the structure of the reconnection layer for different pair multiplicities. In Section 4, we focus on the inflow and outflow motions of the plasma. In Section 5, we discuss the energy partition between magnetic fields and different particle species in the reconnection region. In Section 6, we focus on the evolution of the particle energy spectrum, illustrating how the lepton power-law slope depends on the pair multiplicity. In Section 7, we discuss the astrophysical implications of our findings. We conclude in Section 8, with a summary of our results. Readers interested primarily in the application of our results to jetted AGNs can move directly to Section 7.

2. Numerical Setup

We use the three-dimensional electromagnetic PIC code TRISTAN-MP (Buneman 1993; Spitkovsky 2005) to study magnetic reconnection in pair-proton plasmas. We explore antiparallel reconnection, i.e., we set the guide field perpendicular to the alternating fields to be zero. The reconnection layer is initialized as a Harris sheet of length L, with the magnetic field $\boldsymbol{B} = -B_0 \tanh(2\pi y/\Delta)\hat{\boldsymbol{x}}$ reversing at $y = 0$ over a thickness Δ. Here, we set $\Delta = 80\ c/\omega_p$, where ω_p is the all-species plasma frequency defined in Equation (11), and choose a spatial resolution of $c/\omega_p = 3$ computational cells.

The field strength B_0 is defined through the (total) plasma magnetization $\sigma = B_0^2/4\pi h$, where h is the enthalpy density of the unreconnected plasma including all species (see Equation (4)). The Alfvén speed is related to the magnetization as $v_A/c = \sqrt{\sigma/(\sigma+1)}$. We focus on the regime of relativistic reconnection (i.e., $v_A/c \sim 1$) and explore cases with $\sigma = 1$, 3, and 10 (see Table 1). The proton and pair plasmas outside the layer are initialized with the same temperature ($T_i = T_e$). We consider cases where the pairs are initially relativistically hot ($\Theta_e \equiv kT_e/m_e c^2 = 1$, 10, and 100), but for completeness, we study also a few cases with initially colder pairs ($\Theta_e = 0.1$). In all simulations, the protons are nonrelativistic ($\Theta_i \equiv kT_i/m_i c^2 = \Theta_e m_e/m_i \ll 1$).

Let $N_{\rm ppc}$ denote the total number of computational particles per cell, which is equally partitioned between negatively and positively charged particles. If $q = 2/(\kappa+1)$ denotes the

Table 1
Simulation Parameters

Run	σ	Θ_e	κ	$\sigma_{e,h}$[a]	L/ρ_{Le}	L/ρ_{Li}	$T_{\rm max}$[b]
A0*	1	1	199	2.9	2706.5	13.6	1.8
A1	1	1	66	6.9	1769.0	26.9	1.8
A2	1	1	19	21.4	1004.7	52.9	1.8
A3	1	1	6	69.3	273.2	48.2	6.1[c]
A4*	1	1	6	69.3	557.9	98.4	1.7
A5	1	1	6	69.3	1195.4	210.9	1.3
A6	1	1	3	130.0	398.9	133.0	1.7
A7	1	1	1.2	317.6	257.7	206.6	1.7
A8	1	1	1	387.9	245.2	245.2	5.5
A9	1	1	199	2.9	5799.8	29.1	1.5
B0	1	10	199	1.2	4099.7	20.6	2.0
B1	1	10	66	1.7	3492.7	53.2	1.9
B2	1	10	19	3.4	2466.1	129.8	1.9
B3	1	10	6	9.0	1510.7	266.6	1.8
B4	1	10	3	16.1	1104.6	368.2	1.8
B5	1	10	1	46.4	688.2	688.2	3.1
C1	3	1	199	8.8	1562.6	7.85	1.7
C2	3	1	66	20.7	1021.3	15.5	1.6
C3	3	1	19	64.1	580.1	30.5	1.5
C4*	3	1	6	207.8	322.1	56.8	3.1
C5	3	1	6	207.8	690.2	121.8	1.3
C6	3	1	1	1163.8	141.5	141.5	3.9[c]
D1	3	10	66	5.1	1975.4	30.1	1.2
D2	3	10	19	10.2	1423.8	74.9	1.7
D3	3	10	6	27.1	872.2	153.9	1.5
D4	3	10	1	139.3	397.3	397.3	3.9
E1	10	1	199	29.4	838.4	4.2	1.5
E2	10	1	19	213.6	311.2	16.4	1.4
E3*	10	1	1	3879.2	77.5	77.5	3.9[c]
E4	10	1	1	3879.2	229.8	229.8	1.0
F1	10	10	199	12.9	1296.4	6.5	1.6
F2	10	10	6	90.2	468.0	82.6	1.5
F3	10	10	1	464.5	217.6	217.6	3.9
G1	1	0.1	19	76.4	1230.6	64.8	1.5
G2	1	0.1	3	478.3	491.7	163.9	1.3
H1	1	100	199	1.0	4376.9	22.0	1.9
H2	1	100	19	1.3	3911.1	205.8	2.0
H3	1	100	3	2.7	2610.6	870.2	2.0
H4	1	100	1	6.2	1758.0	1758.0	6.0

Notes. For simulations performed with the same physical parameters but different box sizes, we mark the default cases for display in the figures with an asterisk (*). Simulations with $\kappa = 1$ and $\kappa > 1$ are performed with 4 and 32 computational particles per cell, respectively. In all cases, the plasma skin depth c/ω_p is resolved with three computational cells and the typical domain size is $L/(c/\omega_p) \simeq 5200$–$11200$.

[a] Hot pair plasma magnetization defined in Equation (1).

[b] Duration of the simulation in units of L/c.

[c] The reconnection rate decreases after $\sim 3L/c$ due to the formation of a large boundary island.

physical number ratio of protons to electrons in a plasma with pair multiplicity κ, then the numbers of computational protons and positrons per cell are given, respectively, by $(q/2)N_{\rm ppc}$ and $[(1-q)/2]N_{\rm ppc}$.[6] We varied $N_{\rm ppc}$ from 4 to 64 and checked the convergence of our results in regard to the reconnection rate, outflow four-velocity, and particle energy distributions. For pair-proton simulations with high pair multiplicity (e.g., $\kappa > 10$), we need to use $N_{\rm ppc} > 16$ to achieve convergence (within a few percent in inflow rate and outflow four-velocity), whereas for electron–proton simulations, we find that four particles per cell are sufficient. For cases with high κ (low q), there is a low probability of proton "injection" in a given cell due to the small (physical) fraction of protons per electron. This introduces an appreciable level of shot noise in fluid quantities that are computed from (or governed by) the protons (e.g., outflow four-velocity), which can be mitigated by increasing the number of computational particles per cell.

The magnetic pressure outside the current sheet is balanced by the particle pressure in the sheet. This is achieved by adding a component of hot plasma with the same composition as in the upstream region and overdensity $\eta = 3$ relative to the all-species number density outside the layer. We exclude the hot particles initialized in the current sheet from the particle energy spectra and from all thermodynamical quantities (except the plasma number density), as their properties depend on our choice of the sheet initialization.

Our simulations are performed in a 2D domain, but all three components of the velocity and of the electromagnetic fields are tracked. We adopt periodic boundary conditions in the x direction of the reconnection outflow, and we employ an expanding simulation box in the y direction (i.e., the direction of the reconnection inflow). We also use two moving injectors receding from $y = 0$ along $\pm\hat{\mathbf{y}}$, which constantly introduce fresh magnetized plasma into the simulation domain; for details, see Sironi & Spitkovsky (2011b, 2014), Sironi et al. (2016), Rowan et al. (2017), and Ball et al. (2018). In all cases, the box size along the y direction increases over time; by the end of the simulation, it is comparable to—or larger than—the x extent.

We trigger reconnection at the center of the simulation domain by instantaneously removing the pressure of hot particles that were initialized in the sheet (Sironi et al. 2016; Ball et al. 2018). This causes a central collapse of the current sheet and the formation of two "reconnection fronts" that are pulled along the layer toward the edges of the box by the magnetic tension force and reach the boundaries at $t \sim L/2v_{\rm A}$. The main advantage of this simulation setup is that the results are independent of the initialization of the sheet (i.e., overdensity, temperature, and thickness[7]), in contrast to the untriggered cases where the influence of the initial conditions may affect the temporal evolution of the reconnection rate and the particle energy distributions at early times (see, e.g., Figure 4 of Petropoulou & Sironi 2018).

[6] We fill the cells with particles by performing two cycles of injection. We first inject protons and electrons at equal numbers (i.e., $N_1 = (q/2)N_{\rm ppc}$ per cell) and then inject positrons and electrons, with a number of $N_2 = [(1-q)/2]N_{\rm ppc}$ per cell for each component. The injection is not done on a cell-by-cell basis, but rather in slabs partitioned along the y direction with $N_{\rm cells}$ each, which are handled by different computer cores. When either $N_1 \times N_{\rm cells}$ or $N_2 \times N_{\rm cells}$ is <10, the actual number of particles injected is randomly drawn from a Poisson distribution with mean value equal to $N_1 \times N_{\rm cells}$ or $N_2 \times N_{\rm cells}$, respectively.

[7] This is true if the sheet is thick enough that it does not become spontaneously tearing-unstable at locations that have not been swept up yet by the receding reconnection fronts.

For our typical unit of length, we choose the Larmor radius of electrons (ρ_{Le}) with Lorentz factor equal to the cold pair plasma magnetization ($\sigma_{e,c}$), namely $\rho_{Le} = \sigma_{e,c} m_e c^2/eB_0$, implicitly assuming that reconnection transfers all the magnetic energy to relativistic pairs (for definitions, see Equations (15) and (7)). The proton Larmor radius is defined in a similar way, i.e., $\rho_{Li} = \sigma_{i,c}\, m_i c^2/eB_0$, where $\sigma_{i,c}$ is the cold proton plasma magnetization (see Equation (9)). The size of the computational domain along the reconnection layer L ranges from hundreds to thousands of ρ_{Le} and tens to hundreds of ρ_{Li} (see Table 1). The fact that the Larmor radii change as a function of pair multiplicity is a direct result of our choice to fix the total σ and electron thermal spread Θ_e, as shown in Figure 16 of Appendix A.

A key parameter in our study, as it will become clear in the following sections, is the hot pair plasma magnetization. This is defined as $\sigma_{e,h} \equiv B_0^2/4\pi h_{\pm}$, where $h_{\pm}$ is the enthalpy density of the upstream pair plasma, and it relates to the total σ as

$$\frac{\sigma_{e,h}}{\sigma} = \frac{q\left(\frac{m_i}{m_e} + \Theta_e \frac{\hat{\gamma}_i}{\hat{\gamma}_i - 1}\right) + (2-q)\left(1 + \Theta_e \frac{\hat{\gamma}_e}{\hat{\gamma}_e - 1}\right)}{(2-q)\left(1 + \Theta_e \frac{\hat{\gamma}_e}{\hat{\gamma}_e - 1}\right)}, \quad (1)$$

where $q = 2/(\kappa + 1)$ is the ratio of proton-to-electron number densities and $\hat{\gamma}_{i,e}$ are the adiabatic indices of protons and leptons. Equation (1) can be simplified in the following asymptotic regimes:

1. Relativistically cold electrons ($\Theta_e \ll 1$). Here, $\sigma_{e,h} \approx \sigma[m_i/m_e + \kappa]/\kappa$. For electron–proton plasmas (or in general, if $\kappa \ll m_i/m_e$) this reduces to the well-known result $\sigma_{e,h} \approx \sigma\, m_i/m_e$, whereas for pair-dominated plasmas with $\kappa \gg m_i/m_e$, we find $\sigma_{e,h} \approx \sigma$. Although pairs are cold, if their number density is sufficiently high, like in the latter case, their pressure (which is $\propto \kappa\, \Theta_e$) can be more important than the proton rest-mass energy density.
2. Relativistically hot electrons ($1 < \Theta_e < m_i/m_e$). Here, $\sigma_{e,h} \approx \sigma[m_i/m_e + 4\Theta_e\kappa]/4\Theta_e\kappa$. This reduces to $\sigma_{e,h} \approx \sigma m_i/(4m_e\Theta_e)$ for $\kappa = 1$, while for $\kappa \gg (m_i/m_e)/4\Theta_e$, we find $\sigma_{e,h} \approx \sigma$. In the latter case, the pressure of the hot pairs is large enough to dominate over the rest-mass energy density of protons. Note that the critical pair multiplicity here is lower by a factor of $\sim 4\Theta_e$ compared to the cold electron case (see first bullet point).
3. Relativistically hot protons ($\Theta_e \gg m_i/m_e$). In this ultra-relativistic regime, all fundamental plasma scales (e.g., the plasma frequencies and skin depths) become independent of the particle rest mass. They depend only on the average particle energy—which, in this regime, is similar for protons and pairs. Here, $\sigma_{e,h} \approx \sigma$ independent of κ.

In this study, we focus on cases where the protons are nonrelativistic and dominate the mass density. For the full list of parameters and their definitions, we refer the reader to Appendix A.

3. Structure of the Reconnection Layer

3.1. Temporal Evolution

To illustrate the temporal evolution of the reconnection region, Figure 1 shows snapshots of the 2D structure of the particle number density from one of our simulations in a $\sigma = 1$, $\Theta_e = 1$ pair-proton plasma with pair multiplicity $\kappa = 19$ (A2 in Table 1).

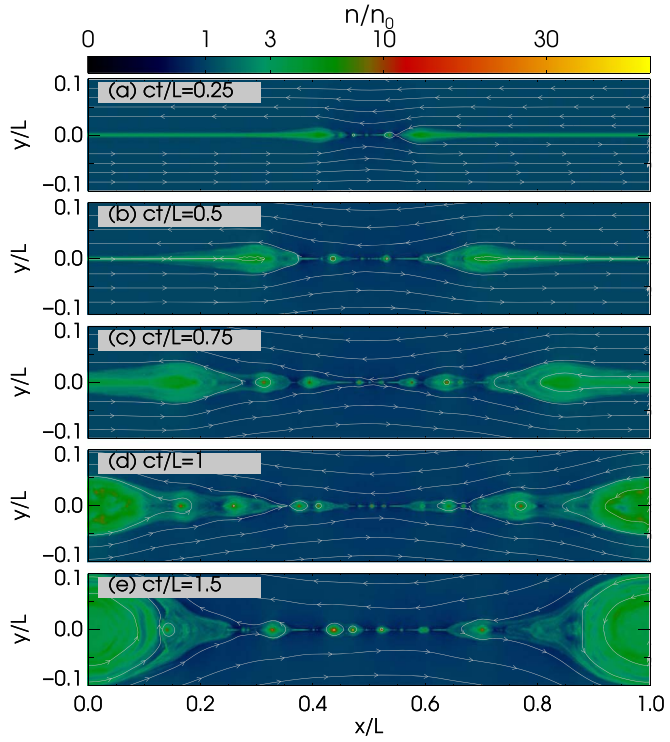

Figure 1. Two-dimensional structure of the all-species particle number density n (normalized to the number density n_0 far from the reconnection layer), from a simulation with $\sigma = 1$, $\Theta_e = 1$, and $\kappa = 19$ (A2 in Table 1). We show only the region $|y|/L < 0.1$ to emphasize the small-scale structures in the reconnection layer (the extent of the computational box along y increases over time, as described in Section 2). The 2D density structure at different times (as marked on the plots) is shown in the panels from top to bottom, with overplotted magnetic field lines (solid white lines). A movie showing the temporal evolution of the 2D structure of the number density of each particle species can be found at https://bit.ly/2HmZR7j.

The localized (at the center) removal of pressure from the hot particle population initialized in the sheet (see Section 2) causes its collapse, thus leading to the formation of a central (or primary) X-point. Two reconnection fronts form on opposite sides of the primary X-point and move outward due to the tension of the magnetic field lines. Plasmoid and secondary X-point formation takes place in the low-density region between the moving fronts, as shown in panels (a) and (b). The fronts reach the boundaries of the simulation domain at $t \approx L/2v_A \approx 0.7L/c$ and form the so-called boundary island, whose size eventually becomes a significant fraction of the layer length (here, $\sim 0.4\,L$ as shown in panels (d) and (e)). The formation of such a large plasmoid, which is the result of periodic boundary conditions, will eventually inhibit the inflow of fresh plasma into the layer, thus shutting off the reconnection process. We verified that the reconnection process remains active[8] for the entire duration of all simulations listed in Table 1, except A3, C6, and E3.

3.2. Dependence on Pair Multiplicity

The effect that the pair multiplicity κ has on the appearance of the reconnection region is illustrated in Figure 2, where 2D snapshots of the all-species particle density, including particles initially present in the sheet, are plotted for increasing values of κ (top to bottom) in plasmas with $\sigma = 1$, $\Theta_e = 1$ (left panel) and $\sigma = 1$, $\Theta_e = 10$ (right panel). In cases with fixed σ and Θ_e but increasing κ, we find that the plasma outflows along the layer become more uniform (i.e., fewer X-points and plasmoids form in the layer) and the typical size of the plasmoids decreases. For fixed σ and κ, an increasing upstream plasma temperature also leads to smaller plasmoids and less fragmentation in the reconnection region (compare left and right panels in Figure 2).

One might argue that the differences in the appearance of the layer as a function of κ are merely a result of the different box sizes in terms of the proton skin depth or alternatively ρ_{Li} (see Table 1). To check this possibility, we compare cases with different physical conditions, but similar box sizes in terms of ρ_{Li}. We find that the plasma conditions have a major effect on the appearance of the layer (for details, see Appendix B) and that the differences seen in Figure 2 are not just a numerical artifact.

Empirically, we find that the most important parameter controlling the appearance of the layer turns out to be $\sigma_{e,h}$. We find that the layer structure is similar for different values of the pair multiplicity and temperature, as long as $\sigma_{e,h}$ is nearly the same. For example, compare panel (e) on the left side to panel (c) on the right side of Figure 2. Typically, the density profile is smoother and the plasmoid sizes are smaller for lower $\sigma_{e,h}$ values[9] (e.g., compare panels (a) and (f) on the left side of Figure 2).

Similar results have been presented by Ball et al. (2018) (see Figure 4 therein) for transrelativistic electron–proton reconnection and an increasing electron plasma β_e, defined as the ratio of upstream electron plasma pressure and magnetic pressure (see Equation (10)). The similarity of our findings is not unexpected, and can be understood as follows: the increasing pair multiplicity corresponds to a decreasing hot pair plasma magnetization $\sigma_{e,h}$ (see Equation (1) and Figure 15), which in turn is inversely proportional to β_e in the limit of $\kappa \gg 1$ (see Equation (10)).

Henceforth, we choose $\sigma_{e,h}$ over β_e to perform our parameter study, because the relative contribution of the rest-mass and internal energy densities to the enthalpy density of the upstream plasma varies among our simulations. In Sections 5 and 6, we will also demonstrate that $\sigma_{e,h}$ is the main parameter that regulates the energy partition and the power-law slope of the lepton energy spectrum.

4. Inflows and Outflows

To compute the reconnection rate in our simulations we average the inflow speed at each time over a slab centered at $x = 0.5\,L$ with width $0.2\,L$ across the layer (i.e., along the y direction) and length $0.5\,L$ (along the x direction). Our results are nearly insensitive to the choice of the slab dimensions as long as the region occupied by the boundary island, where the inflow rate is inhibited, is excluded from the averaging process. The spatially averaged inflow rate is then averaged over time for $t > L/2v_A$, i.e., excluding times when the reconnection fronts are still in the slab.

Our results for simulations with different σ, Θ_e, and κ (Table 1) are presented in Figure 3, where the average inflow speed v_{in} (normalized to v_A) is plotted as a function of the hot pair plasma magnetization $\sigma_{e,h}$. Results for pair-proton and electron–proton cases are indicated with filled and open symbols, respectively. The error bars, which indicate the standard deviation of the reconnection rate over the duration of the simulation, typically become larger with increasing

[8] We characterize the reconnection process as active, as long as the inflow rate of plasma into the reconnection region does not show a monotonically decreasing trend with time and remains $\gtrsim 0.01 v_A$ at all times.

[9] The apparent correlation of the plasmoid size with $\sigma_{e,h}$ is likely related to the dependence of the electron Larmor radius on $\sigma_{e,h}$ (i.e., $\rho_{Le} \propto \sigma_{e,h}^{1/2}$).

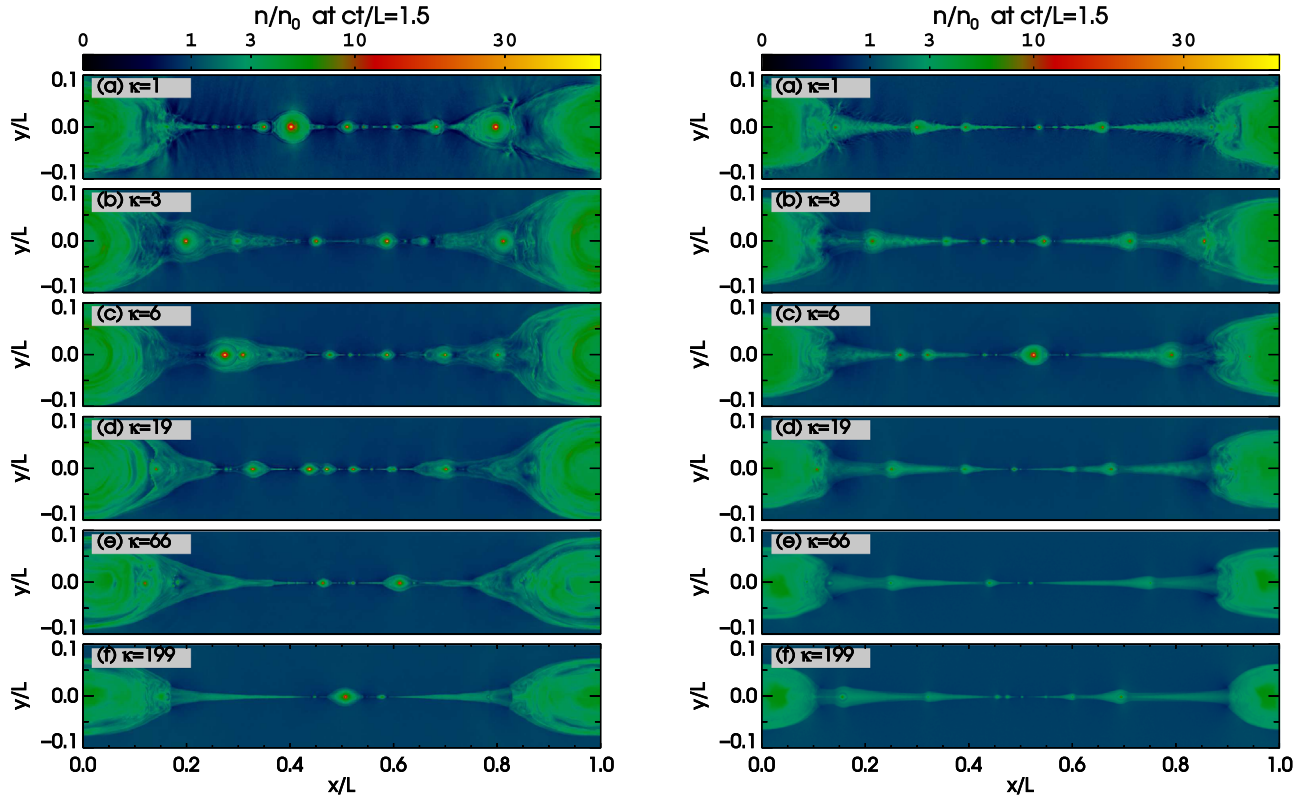

Figure 2. Two-dimensional snapshots of the all-species particle number density n (normalized to the number density n_0 far from the reconnection layer), including the particles initially present in the sheet. Results are displayed at $t = 1.5L/c$ for different values of the pair multiplicity κ, as marked on each panel. The simulations were performed for plasmas with $\sigma = 1$ and $\Theta_e = 1$ (left panel) and $\sigma = 1$ and $\Theta_e = 10$ (right panel); for reference, see cases A0–A2, A4, A6, A8, and B0–B5 in Table 1. The appearance of the layer is similar for cases with similar $\sigma_{e,h}$ values, as exemplified by panels (e) on the left and (c) on the right-hand side of the figure (see also Table 2). Movies showing the temporal evolution of the layer structure for different pair multiplicities can be found at https://bit.ly/2HmZR7j.

$\sigma_{e,h}$ and fixed σ, Θ_e. This suggests that the layer becomes accordingly more structured (see also Figure 2), because the temporal variations of the reconnection rate about its average value relate to the motion and coalescence of plasmoids (see also Petropoulou & Sironi 2018). We find a weak dependence of the average reconnection rate on $\sigma_{e,h}$, as this changes only by a factor of $\sim$3 ($\sim$0.05–0.15) over more than three orders of magnitude in $\sigma_{e,h}$. Despite this weak dependence, our results reveal a clear trend of lower reconnection rates at lower $\sigma_{e,h}$ (i.e., at higher β_e), in agreement with the findings of Ball et al. (2018).

The four-velocity of the plasma outflows in the reconnection region along the x direction, $\Gamma v_{\rm out}/c$, is computed using all particle species, although it is controlled by the protons that contribute most to the plasma inertia. The Lorentz factor Γ takes into account the motion in all three directions, but the bulk motion along x dominates. To estimate the maximum four-velocity, we compute the 95th percentile[10] of all values of $\Gamma v_{\rm out}/c$ at $y = 0$ at each time, and show in Figure 4 its temporal evolution from simulations with $\sigma = 1$, $\Theta_e = 1$, and different pair multiplicities. The outflowing plasma accelerates soon after the onset of reconnection, its motion becomes relativistic, and its maximum four-velocity approaches the asymptotic value $\sqrt{\sigma}$ (Lyubarsky 2005). We note that the 95th percentile of $\Gamma v_{\rm out}/c$ values in the layer provides a more conservative estimate of the maximum outflow four-velocity than the one derived using, for example, the fifth (or tenth) largest value (e.g., Sironi et al. 2016). We verified that, with the latter method, the peak four-velocity is even closer to $\sqrt{\sigma}$. We find no systematic dependence of the maximum outflow four-velocity on the pair multiplicity, apart from the fact that the bulk acceleration is more gradual in plasmas with $\kappa = 199$ (see black line in Figure 4); this is also true for other values of Θ_e and $\sigma = 1$–3.

5. Energy Partition in the Reconnection Region

The question of how the available energy is shared between particles and magnetic fields in the region where plasma has undergone reconnection (henceforth, the reconnection region) is of particular astrophysical importance because it is related to the intensity and spectrum of the associated electromagnetic radiation. Here, we study the energy partition in pair-proton plasmas post-reconnection, as a function of pair multiplicity, magnetization, and temperature of the unreconnected plasma.

To identify the reconnection region, we use a mixing criterion, as proposed by Daughton et al. (2014). Particles are tagged with an identifier (0 or 1) based on their initial location (below or above) with respect to the current sheet. Particles from these two regions get mixed in the course of the reconnection process. We identify the reconnection region by the ensemble of computational cells with mixing fraction above a certain threshold ϵ and below $1 - \epsilon$; here, we employed $\epsilon = 0.01$[11] (for more details, we refer the reader to Rowan et al. (2017) and Ball et al. (2018)). Two-dimensional snapshots of the mixing fraction

[10] We compute the absolute values of the four-velocity measured at different locations along the layer at $y = 0$, sort them in descending order, and determine the value below which 95% of the measurements falls.

[11] We verified that our results are insensitive to the exact value, except for very early times (i.e., $\lesssim 0.15L/c$) where the small size of the reconnection region makes the computation of quantities therein sensitive to the choice of ϵ.

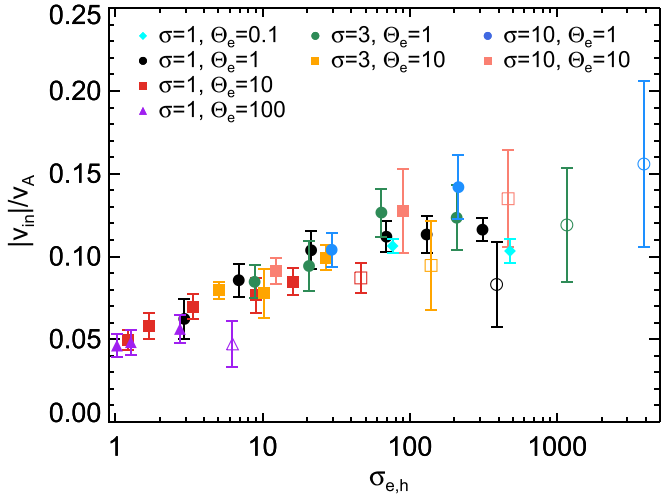

Figure 3. Average inflow rate (in units of the Alfvén speed) as a function of $\sigma_{e,h}$ for all the simulations presented in Table 1 in which the reconnection process is not inhibited by the boundary island. Filled and open symbols are used for simulations in pair-proton and electron–proton plasmas, respectively. Error bars indicate the standard deviation of the spatially averaged inflow rate during the course of the simulation. Results from the box-size scaling simulations are not included here.

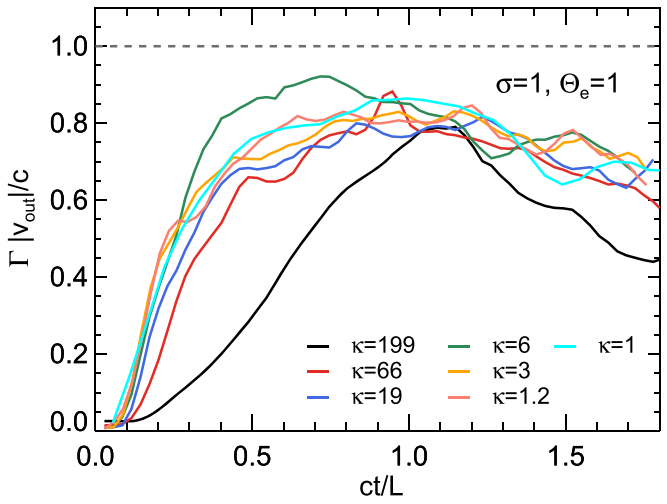

Figure 4. Temporal evolution of the maximum outflow four-velocity (in units of the speed of light) for reconnection in a pair-proton plasma with $\sigma = 1$, $\Theta_e = 1$, and different pair multiplicities marked on the plot (see A0–A2, A4, and A6–A8 in Table 1). At each time, we take a slice at $y = 0$ and use the 95th percentile of all values measured along the layer as a proxy of the maximum four-velocity. The horizontal dashed gray line marks the Alfvén four-velocity. Time is normalized to the light-crossing time of the layer.

from two indicative simulations (see A1 and A6 in Table 1) are presented in Figure 5, where the reconnection region is identified by the mixed colors (green and red).

We compute the kinetic energy of each particle species by summing up the contributions from all computational cells that define the reconnection region, namely $u_j = m_j c^2 \sum_{\rm cells} n_j(\gamma_j - 1)$, where γ_j is the average Lorentz factor of particles of species j in a computational cell. We then normalize u_j to the total energy $u_{\rm tot} = u_B + \sum_{j=i,e^\pm} u_j$, where $u_B = \sum_{\rm cells} B^2/8\pi$. In Figure 6, we show the temporal evolution of $u_j/u_{\rm tot}$ for the same cases as those shown in Figure 5. At very early times, when the reconnection region is small (see gray-shaded region in Figure 6), the plasma properties therein depend on how exactly the reconnection region

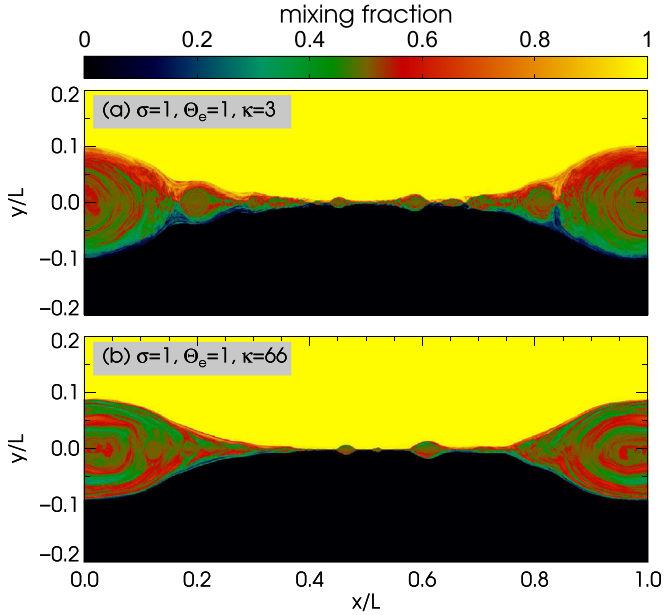

Figure 5. Two-dimensional snapshots of the mixing fraction computed at $t = 1.5L/c$ for two pair-proton simulations with $\kappa = 3$ and $\kappa = 66$ (see A1 and A6 in Table 1).

is identified. However, neither the time-averaged properties nor their late-time evolution are sensitive to the definition of the reconnection region. Given that there might also be other factors affecting the early time evolution (e.g., initial setup), we henceforth ignore this transitional early period. At later times, the ratio of post-reconnection magnetic energy to the total energy decreases gradually with time, whereas the pair energy density ratio reaches an almost constant value very soon after the onset of reconnection (i.e., already at $0.4L/c$). The proton energy ratio typically asymptotes to a constant value at later times compared to the pairs, but our simulations are long enough to capture the steady-state values of all energy ratios. We find similar temporal trends for other cases as well.

The time-averaged energy ratios of protons, pairs, and magnetic fields in the reconnection region are presented in Figure 7. The leftmost point in each series with a given color corresponds to pair-proton plasmas with $\kappa = 199$, and the rightmost point corresponds to the pure electron–proton case with $\kappa = 1$ (open symbols). The fraction of energy that remains in the post-reconnection magnetic field is $\sim 1/3$ and is approximately constant for a wide range of $\sigma_{e,h}$ values, spanning almost three orders of magnitude (bottom panel). Only for $\sigma_{e,h} < 3$, we find subequipartition values, i.e., $u_B/u_{\rm tot} < 1/3$. In this parameter regime, the pairs in the plasma carry most of the upstream total energy. Upon entering the reconnection region, the pair kinetic energy increases even further, at the expense of magnetic energy, due to field dissipation. As a result, the post-reconnection magnetic energy for $\sigma_{e,h} < 3$ is only a small fraction of the total energy ($u_B/u_{\rm tot} \sim 0.1$–0.2).

One can empirically define two regimes of interest for the particle energy ratios: a low-$\sigma_{e,h}$ regime ($\sigma_{e,h} \lesssim 30$), where $u_i/u_{\rm tot} \propto \sigma_{e,h}$ and $u_{e^\pm}/u_{\rm tot} \propto \sigma_{e,h}^{-1/2}$, and a high-$\sigma_{e,h}$ regime ($\sigma_{e,h} > 30$), where both ratios are almost independent of the hot pair plasma magnetization. In both regimes, there is no dependence of the particle energy ratios on Θ_e, but a weak dependence on the total plasma magnetization σ is evident. This can be seen more

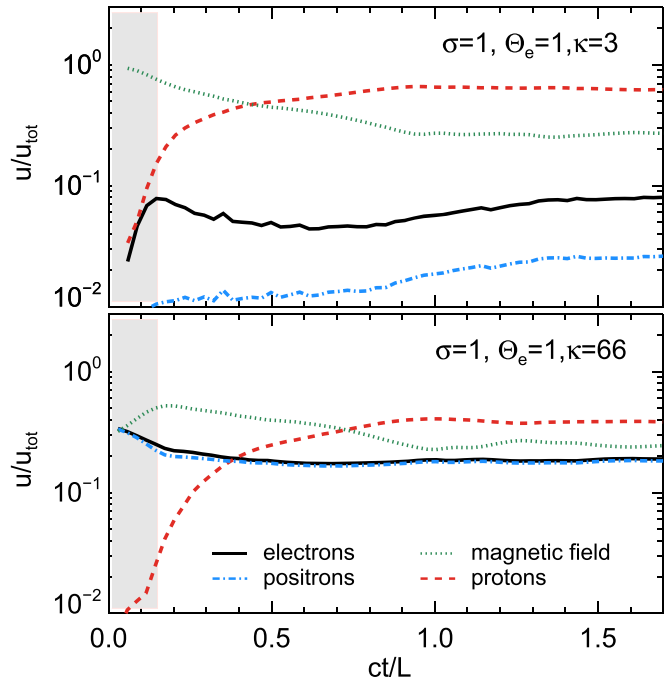

Figure 6. Temporal evolution of the energy stored in magnetic field (dotted green line), protons (dashed red line), electrons (solid black line), and positrons (dashed–dotted blue line) in the reconnection region. The energies of all components are normalized to the total (particle and magnetic) energy at each time. Results for $\kappa = 3$ and $\kappa = 66$ are shown in the top and bottom panels. Snapshots of the mixing fraction used to identify the reconnection region are shown in Figure 5. The early-time evolution of the energy ratios (gray-shaded region) is sensitive to the choice of the mixing threshold.

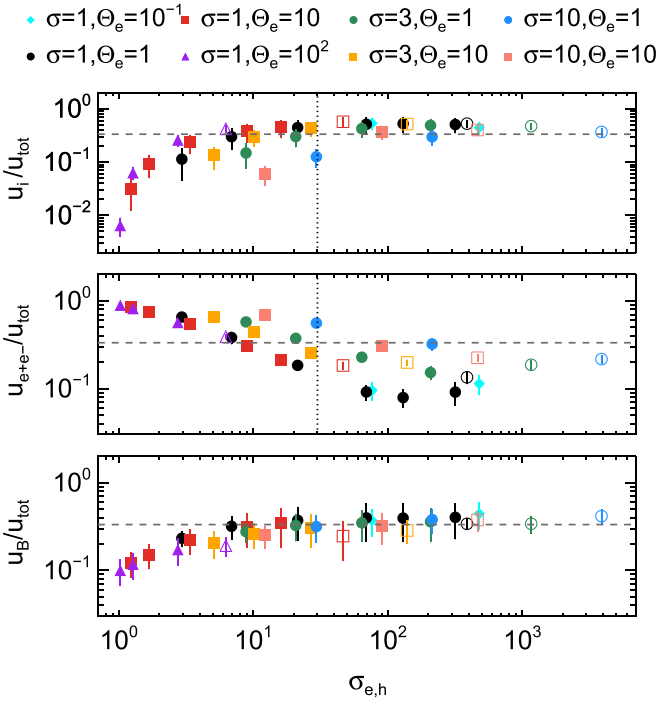

Figure 7. Time-averaged energy ratios of protons (top panel), pairs (middle panel), and magnetic field (bottom panel) in the reconnection region, plotted against $\sigma_{e,h}$ for our complete set of simulations with different physical parameters marked on the plot (same color coding used as in Figure 3). Results from the size-scaling simulations are not included here. Filled and open symbols are used for simulations in pair-proton and electron–proton reconnection, respectively. Error bars indicate the standard deviation of the energy ratios during the course of the simulation. In all panels, the horizontal dashed line marks the equipartition value of one-third. The dependence of the particle energy ratios on $\sigma_{e,h}$ changes at $\sigma_{e,h} \sim 30$, as noted by the dotted vertical line in the upper two panels.

clearly in the middle panel of Figure 7, where points with the lowest σ (black and cyan symbols) systematically lie below points with higher σ. Finally, energy equipartition between magnetic fields, protons, and pairs is asymptotically achieved for $\sigma \gg 1$ and $\sigma_{e,h} \gtrsim 30$, with each component carrying $\sim 1/3$ of the total energy.

The dependence of the particle energy densities on $\sigma_{e,h}$ could originate from either changes in the number density or in the mean particle Lorentz factor, or both. A proxy of the average post-reconnection particle Lorentz factor, $\langle \gamma_j - 1 \rangle = \sum_{\rm cells} u_j / \sum_{\rm cells} n_j m_j c^2$, is plotted against $\sigma_{e,h}$ in the left panel Figure 8 for protons (top panel) and pairs (bottom panel). In all cases, we find that the post-reconnection mean proton Lorentz factor is almost independent of $\sigma_{e,h}$ and Θ_e, but has a dependence on σ, with larger values leading to higher mean proton Lorentz factors. Indeed, when $\langle \gamma_i - 1 \rangle$ is normalized to $\alpha_i \sigma$ (with $\alpha_i = 1/3$ for $\sigma = 1, 3$ and $\alpha_i = 1/5$ for $\sigma = 10$) all curves coincide, as shown in the right panel of Figure 8. In contrast to the protons, the mean lepton Lorentz factor depends on Θ_e, σ, and $\sigma_{e,h}$, as shown in the left panel of Figure 8. For $\sigma \geqslant 1$, we empirically find that the mean lepton Lorentz factor can be approximated as (see also right panel in Figure 8)

$$\langle \gamma_e - 1 \rangle \approx \sqrt{\sigma}(1 + 4\Theta_e)\left(1 + \frac{\sigma_{e,h}}{30}\right). \quad (2)$$

The asymptotic value of the mean lepton Lorentz factor for $\sigma_{e,h} \ll 30$ implies that, in this regime, the pairs in the reconnection region still bear memory of their initial (pre-reconnection) conditions (in particular, of Θ_e), in agreement with the discussion on Figure 7. In the high-$\sigma_{e,h}$ regime, the mean lepton Lorentz factor scales almost linearly with $\sigma_{e,h}$. This asymptotic behavior of $\langle \gamma_e - 1 \rangle$ can be understood as follows. For fixed σ and Θ_e (i.e., fixed amount of post-reconnection energy available for the particles), the energy per lepton increases as the number of leptons per proton decreases, or equivalently, as $\sigma_{e,h}$ increases (see also Equation (1)). We refer the reader to Appendix D, for a quantitative discussion on the dependence of the mean lepton Lorentz factor on the physical parameters σ, Θ_e, and κ of the upstream plasma.

6. Particle Energy Distributions

Having discussed the general properties of reconnection in pair-proton plasmas (see Sections 3–5), we continue our study by examining the particle energy distributions and their dependence on physical parameters, most notably on $\sigma_{e,h}$.

6.1. Temporal Evolution of Particle Energy Spectra

The energy distribution of each particle species is defined as $f_j(E) \equiv dN_j/dE$, where E is the particle kinetic energy and $j = i, e^-, e^+$. Henceforth, all particle energies are kinetic (i.e., excluding rest mass), unless stated otherwise.

As a representative example, Figure 9 presents the temporal evolution of the electron, positron, and proton energy distributions (from top to bottom) from a simulation with $\sigma = 1$, $\Theta_e = 1$, and $\kappa = 19$ (see also Figure 1, for a depiction of the layer structure). The energy distributions of each particle

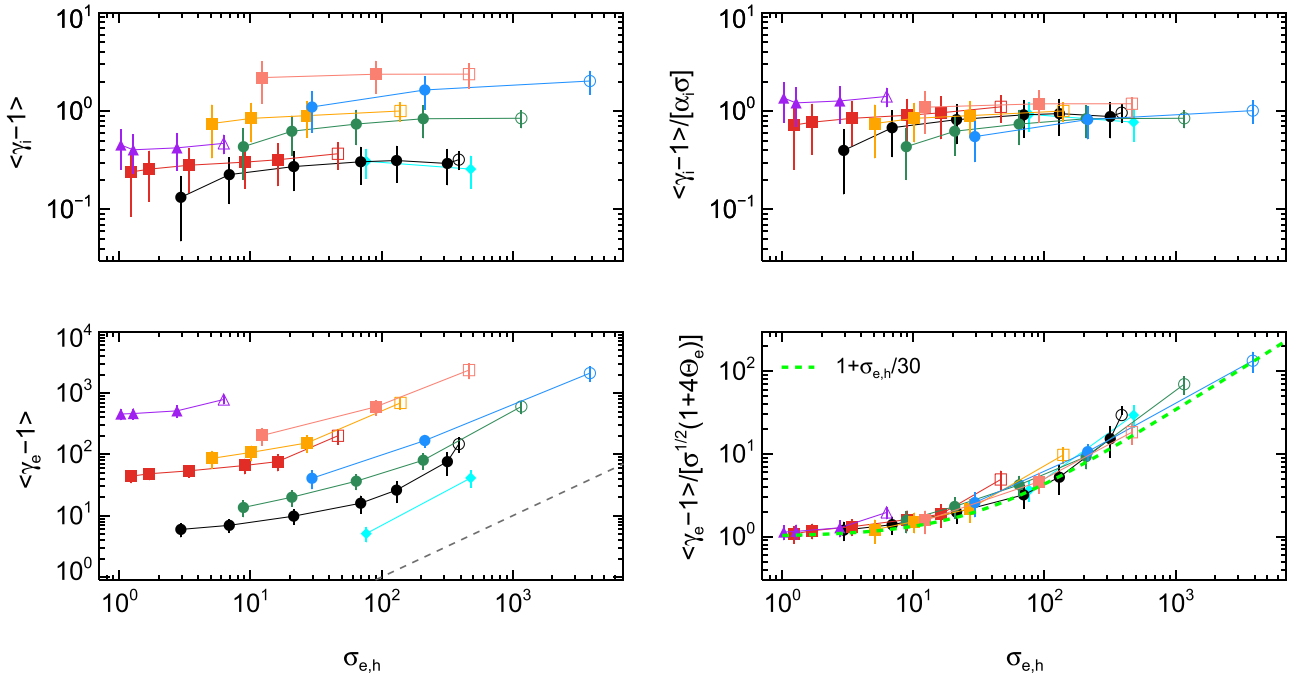

Figure 8. Left panel: time-averaged ratios of the energy density to the rest mass energy density of protons (top panel) and pairs (bottom panel), which serve as a proxy of $\langle \gamma_j - 1 \rangle$. A dashed line with slope unity is also plotted in the bottom panel to show the linear asymptotic dependence of the mean lepton Lorentz factor on $\sigma_{e,h}$. All symbols have the same meaning as in Figure 7. Right panel: proxy of the post-reconnection particle Lorentz factor normalized to $\alpha_i\sigma$ for protons (with $\alpha_i = 1/3$ for $\sigma = 1$, 3 and $\alpha_i = 1/5$ for $\sigma = 10$) and $\sqrt{\sigma}(1 + 4\Theta_e)$ for leptons.

species are normalized to the total number of particles of that species in the reconnection region at the end of the simulation. The displayed spectra exclude the particle population that was initialized in the current sheet. For reference, the spectrum obtained at the time the reconnection fronts reach the boundaries (i.e., $t = L/2v_A$) is shown with a dashed black line.

Soon after the onset of reconnection, the electron and positron energy spectra in the reconnection region begin to deviate from their initial Maxwell–Jüttner distributions. They develop a nonthermal component even before the time the reconnection fronts reach the boundaries of the layer (i.e., at $ct/L \sim 0.7$). The nonthermal part of the spectrum of pairs can be described by a power law above a characteristic energy where the post-reconnection energy spectrum $Ef_j(E)$ obtains its peak value. For the adopted parameters, we find $E_{\rm pk,}e/m_e c^2 \sim 10$, in agreement with the value of the mean post-reconnection Lorentz factor that we derived in Section 5 (see third black symbol from the left in bottom panel of Figure 8).

There is a clear difference between the temporal evolution of the lepton and proton energy distributions. More specifically, the nonthermal component of the proton spectrum begins to emerge only at $t > L/2v_A$, after the fronts have reached the boundaries. At earlier times, the proton energy spectrum shows a narrow peak that evolves with time. We interpret this early-time spectral feature as a result of heating and bulk motion of the proton plasma, whose outflow four-velocity evolves strongly for $t < 0.5L/c$ (see blue curve in the top panel of Figure 4). Similar results were obtained by Ball et al. (2018) for transrelativistic reconnection in electron–proton plasmas (see Figure 3 therein).

The late-time development of the power law in the proton distribution can be understood in terms of the interactions of particles with various structures in the layer. X-points are

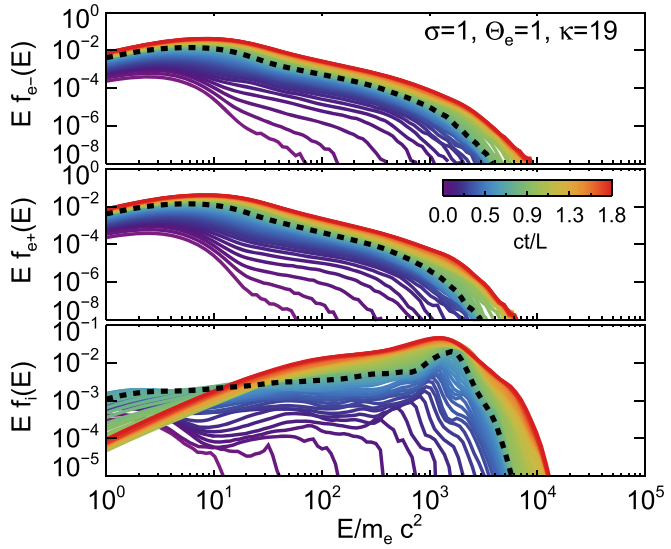

Figure 9. Temporal evolution (see inset color bar) of the electron, positron, and proton energy distributions (from top to bottom) extracted from the reconnection region of a simulation with $\sigma = 1$, $\Theta_e = 1$, and $\kappa = 19$; see also Figure 1, for a depiction of the layer structure. The spectrum obtained at the time the reconnection fronts reach the boundaries (i.e., $t = L/2v_A$) is highlighted with a dashed black line. The energy distributions of each particle species are normalized to the total number of particles of that species within the reconnection region at the end of the simulation.

typically smaller than the proton Larmor radius, so direct proton acceleration by the nonideal reconnection electric field is not very efficient. We find evidence of proton acceleration only when the boundary island, which is the largest structure in the layer, begins to form. We argue that, in a much larger simulation domain, where larger secondary plasmoids could

form, protons should show signs of acceleration even before the reconnection fronts interact with the boundaries.

6.2. Effects of Pair Multiplicity

To illustrate the dependence of the particle energy distributions on pair multiplicity, Figure 10 shows the energy spectra from a set of simulations with $\sigma = 1$, $\Theta_e = 1$ and different values of κ marked on the plots. Thick solid and thin dashed lines show the spectra from the reconnection region and the whole simulation domain, respectively. The spectra are computed at the end of each simulation and are normalized to the total number of protons within the reconnection region. The vertical dashed–dotted line in each panel marks the energy of particles with Larmor radius[12] 0.1 L, i.e., comparable to the size of the largest plasmoids in the layer.

The peak energy of the pair energy distributions depends strongly on the pair multiplicity for $\kappa < 6$, and becomes approximately constant (here, $E_{\rm pk,e}/m_e c^2 \sim 10$) for higher pair multiplicities. In contrast, the peak proton energy is approximately constant for all κ values we explored. The dependence of the peak particle energy on κ is more clearly illustrated in Figure 11, where the energy distributions of each particle species are plotted for different values of κ. These findings are in agreement with those presented in Figure 8 for the mean particle Lorentz factor. The fact that the mean and the peak lepton energies are comparable is not surprising: most of the energy is expected to reside at the peak of the energy distribution, given that the power-law slopes of the lepton energy spectra are typically $\gtrsim 2$ (see below and Section 6.3).

Above the peak energy $E_{\rm pk,e}$, the pair energy spectra can be approximated by a power law with slope p (i.e., $f(E) \propto E^{-p}$) followed by a cutoff. The power-law segment used for the estimation of the slope (see Section 6.3) is overplotted (dashed–dotted blue lines) in order to guide the eye. Inspection of the figure (see also Figure 11) shows that the power law of the pair distributions becomes steeper (i.e., larger p values) as the pair multiplicity increases (for details, see Section 6.3). The power law of the pair distributions extends well beyond their peak energy for all the cases we explored, except for the cases with the highest Θ_e, which are discussed in Appendix E. For protons, a well-developed power law forms only for small pair multiplicities (here, for $\kappa < 19$), while their energy distribution shows a steep drop above the peak energy $E_{\rm pk,i}/m_e c^2 \sim 10^3$ for $\kappa = 66$ and 199. This should not be mistakenly interpreted as a limitation of reconnection in accelerating protons in plasmas with high pair multiplicities. It is merely a result of the limited size of the computational domain in terms of the proton Larmor radius: L/ρ_{Li} drops by a factor of 10 between the simulations with $\kappa = 3$ and $\kappa = 199$, as shown in Table 1 (the dependence of the particle energy distributions on the box size is discussed in Appendix C). For these reasons, we do not attempt to study the spectral properties of the proton energy distributions, and in what follows, we focus on the energy distributions of pairs.

6.3. Power-law Slope of Pair Energy Spectra

We compute the slope of the power-law segment of the pair energy distributions and explore its dependence on the physical parameters. Due to the similarity between the energy distributions of positrons and electrons (see Figure 10) it is sufficient to use one of the two to compute the slope. For this purpose, we henceforth use the electron energy spectrum obtained at the end of each simulation.

The electron energy distribution can be generally described by two components: a low-energy broad component that forms due to heating and a high-energy component, which can be described as a truncated power law at low energies with an exponential cutoff at higher energies (e.g., panels in middle row of Figure 10). A detailed fit to the simulation data is very challenging due to the degeneracy in the model parameters describing the two components. For example, the choice of the low-energy end of the power law affects the broadness and normalization of the low-energy component and vice versa. The slope inferred from the two-component fit to the data can vary by 0.2 at most, depending on the other model parameters. Given the inherit uncertainties in the fitting procedure, in what follows, we identify the power-law segment by eye and fit it with a single power law (see dashed–dotted blue lines in Figure 10).

The extent of the power law is, in most cases, sufficient to allow a reliable estimation of its slope. We assign a systematic error of ± 0.2 to the derived slope, which dominates the statistical error from the fits, to account for the subjective choice of the fitting energy range. For those simulations with much greater duration than the others (see electron–proton cases in Table 1), we also computed the slope at earlier times (i.e., comparable to the duration of all other cases) and found no difference in the inferred p value within the systematic error. Although a hard power law can be safely distinguished from the thermal part of the energy distribution, for very steep power laws with $p \gtrsim 4$, we cannot exclude the possibility that what we are identifying as a power law is in fact the tail of a thermal-like distribution or a multitemperature distribution (see e.g., bottom right panel in Figure 10). Detailed modeling of the energy distributions, which is important for determining the temporal evolution of the cutoff energy or the shape of the exponential cutoff (Werner et al. 2016; Kagan et al. 2018; Petropoulou & Sironi 2018), lies beyond the scope of this paper.

Our results are summarized in Figure 12 and Table 2, where the slope of the electron energy distribution p is plotted as a function of $\sigma_{e,h}$. We do not include the results from runs H1–H3 with the highest plasma temperature (see Table 1), because the energy spectra are qualitatively different from all other cases; for details, see Appendix E and Ball et al. (2018). The inferred power-law slopes fall onto two branches (dashed gray lines) that track each other for $\sigma_{e,h} \sim 30$–300, but merge in the asymptotic regime of $\sigma_{e,h} \gtrsim 10^3$, where both protons and pairs start to behave as one particle species (i.e., their Larmor radii become similar). The upper branch (i.e., larger p values) is composed of results from $\kappa = 1$ simulations, whereas results for larger multiplicities ($\kappa \gtrsim 6$) fall onto the lower branch (i.e., smaller p values). For a fixed pair of Θ_e and σ values, a transition from the lower to the upper branch, which is accompanied by a steepening of the power law, occurs at $\kappa \sim 3$–6. No transition is found for $\sigma = 10$. The power-law slopes derived for the majority of the simulations lie on the lower branch for a wide range of $\sigma_{e,h}$ values, spanning more than three orders in magnitude, despite the differences in the total plasma magnetization, temperature, and pair multiplicity. This suggests that $\sigma_{e,h}$ is a key physical parameter in regard to the pair energy distribution.

[12] The Larmor radius is computed using the upstream magnetic field strength.

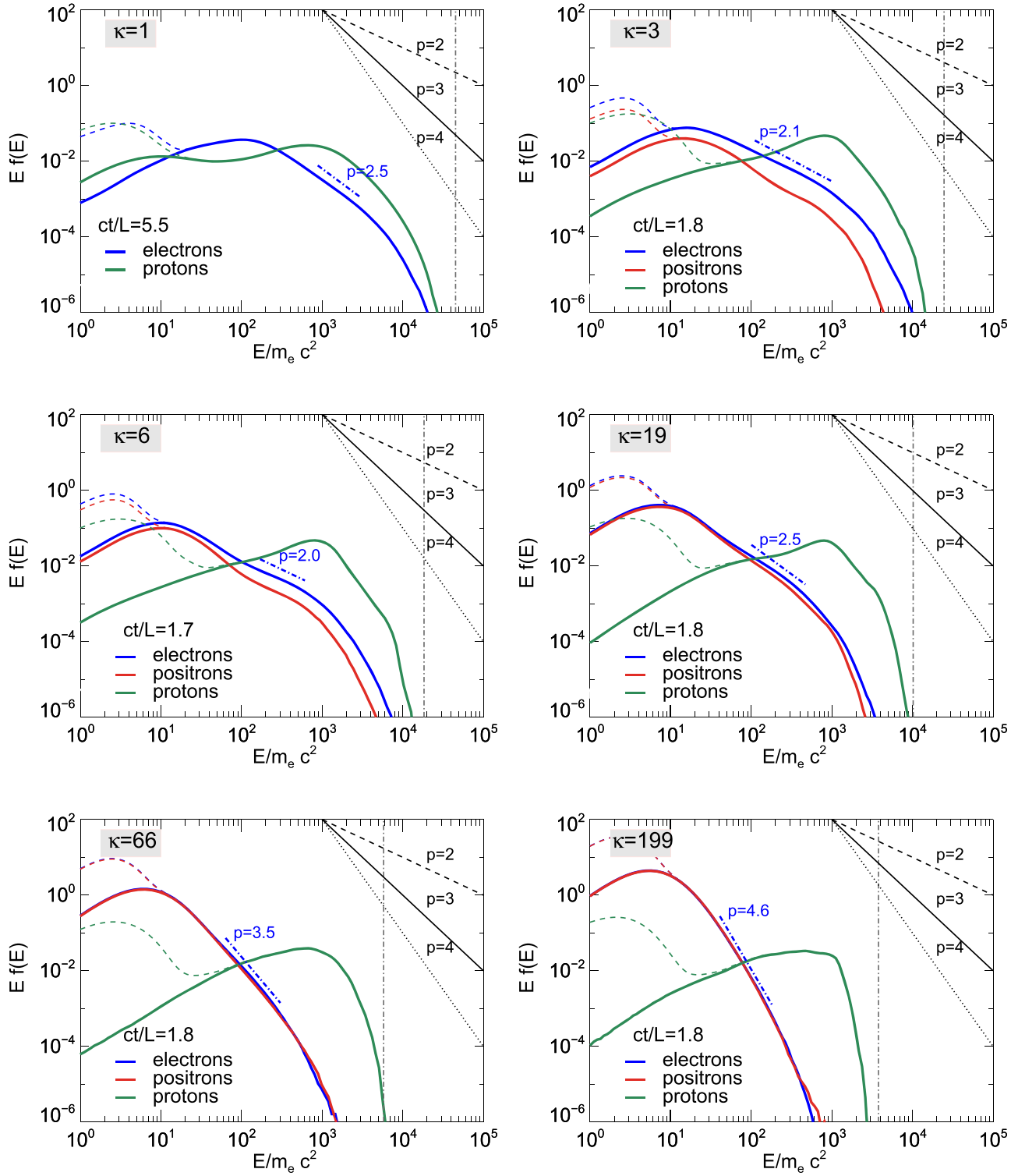

Figure 10. Electron (blue lines), positron (red lines), and proton (green lines) energy distributions computed from a set of simulations with $\sigma = 1$, $\Theta_e = 1$, and different pair multiplicities marked on the plots (see runs A0–A2, A4, A6 and A8 in Table 1). The spectra are computed at the end of each simulation and are normalized to the total number of protons within the reconnection region at that time. Thick solid and thin dashed lines show the spectra from the reconnection region and the whole simulation domain, respectively. The power-law segment of the electron distributions used to measure the slope is indicated with dashed–dotted blue lines. The black lines in the upper right corner of each panel have slopes of $-p + 1$ and are plotted for three values of p in order to facilitate the comparison with the power-law segments of the particle distributions. The vertical dashed–dotted line in each panel marks the energy of relativistic particles with Larmor radius 0.1 L.

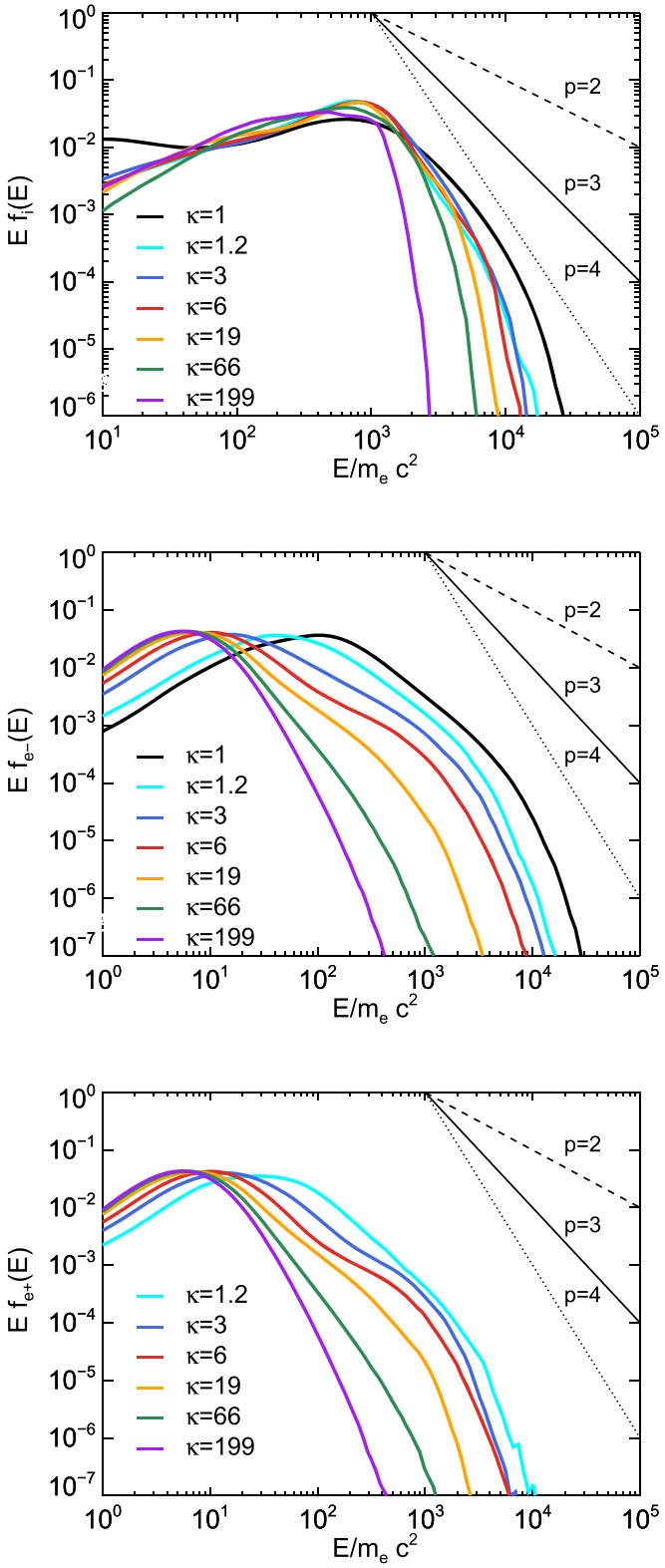

Figure 11. Post-reconnection energy distributions of protons, electrons, and positrons (from top to bottom) from simulations with $\sigma = 1$, $\Theta_e = 1$, and different pair multiplicities marked on each plot (see runs A0–A2, A4, and A6–A8 in Table 1). The spectrum of each particle species is computed at the end of each simulation and is normalized to the total particle number of that species in the reconnection region. The black lines in the upper right corner of each panel have slopes of $-p + 1$ and are plotted for three values of p in order to facilitate the comparison with the power-law segments of the particle distributions.

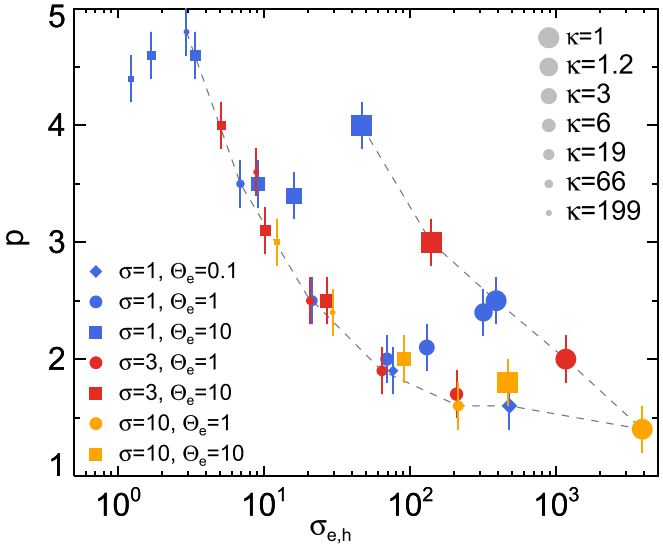

Figure 12. Power-law index of the electron energy distribution p as a function of $\sigma_{e,h}$ from our simulations presented in Table 1 (results from the box-size scaling runs are not included). Different symbols, colors, and symbol sizes are used to indicate simulations with different values of Θ_e, σ, and κ, respectively (see inset legends). Dashed gray lines indicate the two branches discussed in text. A systematic error of ± 0.2 applies to all p values (for details, see Section 6.3).

In general, higher $\sigma_{e,h}$ lead to the production of harder power laws (i.e., smaller p values), which is similar to the trend reported by Ball et al. (2018) for a decreasing electron plasma β_e in electron–proton reconnection (see Figure 13 therein). By tracking a large number of particles, Ball et al. (2018) showed that, at low β_e, particles primarily accelerate via the nonideal electric field at X-points. Because their number was found to decrease with increasing β_e, the authors argued that lower acceleration efficiencies and steeper power laws are expected at high β_e. The dependence of our derived power-law slopes on $\sigma_{e,h}$ can be qualitatively understood in the same context, because more X-points and secondary plasmoids are formed (see Section 3.2) at high $\sigma_{e,h}$ (or equivalently low β_e). A quantitative description of our results requires a detailed study of the electron acceleration, which is beyond the scope of this paper.

7. Astrophysical Implications

In this section, we discuss the findings of our simulations in the context of AGN jets. We focus on blazars, the most extreme subclass of AGN, with jets closely aligned to our line of sight. The blazar jet emission has a characteristic double-humped shape with a broad low-energy component extending from radio wavelengths up to UV or X-ray energies, and a high-energy component extending across the X-ray and γ-ray bands (Ulrich et al. 1997; Fossati et al. 1998; Costamante et al. 2001). The low-energy hump is believed to be produced by synchrotron emission of relativistic pairs with a power-law (or broken power-law) energy distribution (e.g., Celotti & Ghisellini 2008), which is suggestive of nonthermal particle acceleration. The synchrotron-emitting pairs can also inverse Compton scatter low-energy photons to γ-ray energies, which could explain the high-energy component of the blazar

Table 2
Values of Physical Quantities Displayed in Figures 12 and 13. The Electron Plasma Parameter, Defined by Equation (10), is also Listed

Run	σ	Θ_e	κ	$\sigma_{e,h}$	β_e	p	$\langle\gamma_e - 1\rangle$
A0	1	1	199	2.9	0.072	4.8	6.0
A1	1	1	66	6.9	0.031	3.5	7.0
A2	1	1	19	21.4	0.010	2.5	9.8
A4	1	1	6	69.3	0.003	2.0	15.8
A6	1	1	3	130.0	0.002	2.1	25.8
A7	1	1	1.2	317.6	0.001	2.4	75.0
A8	1	1	1	387.9	0.001	2.5	147.5
B0	1	10	199	1.2	0.199	4.4	44.1
B1	1	10	66	1.7	0.146	4.6	48.2
B2	1	10	19	3.4	0.076	4.6	53.9
B3	1	10	6	9.0	0.032	3.5	65.9
B4	1	10	3	16.1	0.020	3.4	76.3
B5	1	10	1	46.4	0.010	4.0	201.3
C1	3	1	199	8.8	0.024	3.6	13.6
C2	3	1	66	20.7	0.010	2.5	20.0
C3	3	1	19	64.1	0.003	1.9	36.3
C4	3	1	6	207.8	0.001	1.7	79.8
C6	3	1	1	1163.8	0.0004	2.0	602.9
D1	3	10	66	5.1	0.049	4.0	86.0
D2	3	10	19	10.2	0.025	3.1	107.9
D3	3	10	6	27.1	0.011	2.5	153.7
D4	3	10	1	139.3	0.003	3.0	691.2
E1	10	1	199	29.4	0.007	2.4	40.6
E2	10	1	19	213.6	0.001	1.6	166.3
E3	10	1	1	3879.2	0.0001	1.4[a]	2114.7
F1	10	10	199	12.9	0.020	3.0	203.1
F2	10	10	6	90.2	0.003	2.0	592.4
F3	10	10	1	464.5	0.001	1.8	2371.3
G1	1	0.1	19	76.4	0.001	1.9	0.31
G2	1	0.1	3	478.3	0.0002	1.6	0.25
H1	1	100	199	1.0	0.244	3.2	454.0
H2	1	100	19	1.3	0.205	3.3	463.1
H3	1	100	3	2.7	0.121	3.6	512.2

Note. A systematic error of ± 0.2 applies to all p values. Results from the box-size scaling simulations are not included here.

[a] The power law might not have reached saturation, because this is the smallest box-size simulation in terms of ρ_{Le} (see Table 1) and the power laws tend to become steeper with increasing box size (Ball et al. 2018; Petropoulou & Sironi 2018). To check this, we ran a simulation with a box three times larger (E4 in Table 1) and found a slope of 1.6, which is comparable to the reported value within the systematic uncertainties.

spectrum.[13] In blazars with TeV γ-ray emission, electrons should accelerate up to Lorentz factors 10^5–10^6 to explain the highest photon energies (e.g., Aleksić et al. 2012; Ahnen et al. 2018).

7.1. Properties of Radiating Particles

A key parameter in blazar emission models is the shape of the nonthermal pair distribution (e.g., power law, broken power law, log-parabolic, and others). The assumed distribution in most cases is phenomenological, as it is not derived from a physical scenario. Upon adopting a specific model for the energy distribution of accelerated pairs, its properties (e.g., power-law slope, minimum, and maximum Lorentz factors) are inferred by modeling the broadband blazar photon spectrum (e.g., Celotti & Ghisellini 2008; Ghisellini et al. 2014). However, not all the model parameters can be uniquely determined, due to degeneracies that are inherent in the radiative models (e.g., Cerruti et al. 2013).

Bearing in mind the aforementioned caveats, we continue with a tentative comparison of our results (see Sections 5–6) with those inferred by radiative leptonic models. As an indicative example, we use the results of Celotti & Ghisellini (2008). The accelerated lepton distribution that was used for the modeling was assumed to be a broken power law:

$$f(\gamma) \propto \begin{cases} \gamma^{-s_1}, & \gamma \leqslant \gamma_{inj} \\ \gamma^{-s_2}, & \gamma > \gamma_{inj} \end{cases} \quad (3)$$

where $s_1 = 1$, and s_2, γ_{inj} were determined by the fit to the data. There is some degeneracy in the low-energy index, because distributions with even flatter spectra than the one above (i.e., $s_1 < 1$) cannot be usually distinguished by the data (see also Ghisellini et al. 2014).

In our simulations, we find that the post-reconnection pair energy distributions exhibit a power law extending well beyond a broad thermal-like component that peaks at $E_{\rm pk,e}$ (e.g., Figures 10 and 11). At $E < E_{\rm pk,e}$, the pair spectra in the reconnection region generally follow the low-energy tail of a Maxwell–Jüttner distribution (e.g., Figure 23), which can be modeled by an inverted power law (i.e., $s_1 < 0$). For the purpose of making a general comparison to the modeling results, we can phenomenologically describe the lepton energy spectra from our simulations via Equation (3), with $s_1 < 1$, $s_2 = p$, and a peak Lorentz factor $\gamma_{inj} = 1 + E_{\rm pk,e}/m_e c^2$, which depends on the total magnetization and temperature of the plasma (e.g., Figures 10 and 23). Using the fitting results of Celotti & Ghisellini (2008) (see Table A1 therein), we compute the mean Lorentz factor of the accelerated distribution (i.e., without radiative cooling) and compare it against the one determined by our simulations (e.g., Figure 8).

Our results are summarized in Figure 13, where the power-law index p above the peak Lorentz factor of the distribution is plotted against the mean Lorentz factor $\langle\gamma_e\rangle$ of the distribution (for a tabulated list of our results, see Table 2). Open and filled triangles indicate the values from the leptonic modeling of Celotti & Ghisellini (2008) for FSRQs and BL Lac objects, respectively. The predictions of reconnection are shown with colored symbols (for details, see figure caption). The degeneracy of the power-law index p on the physical parameters, such as σ and Θ_e shown in Figure 12, is lifted when p is plotted against the mean lepton Lorentz factor. This is illustrated in Figure 13, where, for fixed σ, curves corresponding to higher Θ_e values are shifted toward larger $\langle\gamma_e\rangle$ and p values (upper right corner of the plot). For fixed plasma temperature but increasing σ, the curves are shifted toward lower p values (i.e., harder power laws) and larger mean particle energies, regardless of the pair multiplicity.

Interestingly, the values from our simulations fall in the same range with those inferred by leptonic radiation models. More specifically, the numerically obtained curves for $\Theta_e = 1$ and 10 enclose most of the results for FSRQs (open triangles). One can envision different families of curves that pass through the data points for FSRQs, which can be obtained by simply changing the temperature of the upstream plasma from $\Theta_e = 1$ to 10. For example, some FSRQ results could be interpreted in the context of reconnection in pair-proton plasmas with $\Theta_e = 3$, $\sigma = 1$, and $\kappa \sim 1$–10 (imagine the blue line with circles shifted to the right and upward). The relevant range of multiplicities would be somewhere between $\sim$10 and 70, for $\Theta_e = 3$ and $\sigma = 3$ (imagine the red line with circles shifted to the right and upward). We find that reconnection in cold pair-proton plasmas

[13] This is true in leptonic scenarios where the broadband jet emission is attributed to relativistic pairs. This is our working hypothesis, and our results should be interpreted in this framework.

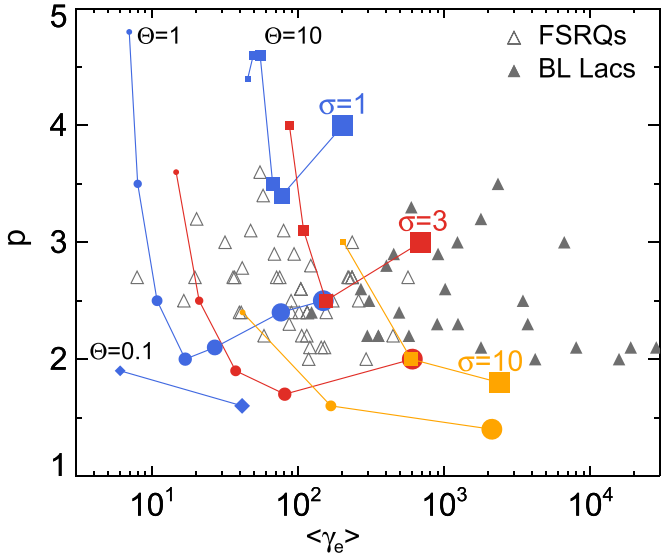

Figure 13. Power-law index of the electron distribution p plotted against the mean electron Lorentz factor $\langle\gamma_e\rangle$ from our simulations. Different colors and symbols are used to indicate the total plasma magnetization σ and temperature Θ_e, respectively. The pair multiplicity κ is indicated by the symbol size, as in Figure 12. A systematic error of ± 0.2 applies to all p values, but to avoid visual clutter, it is not illustrated. Overplotted with filled and open triangles are the values inferred by leptonic modeling of blazar broadband spectra (Celotti & Ghisellini 2008) for different blazar types (see inset legend).

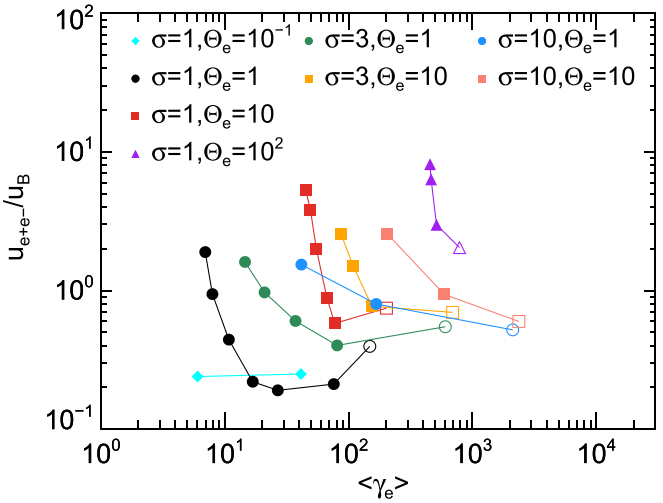

Figure 14. Ratio of post-reconnection lepton-to-magnetic energy densities plotted against the mean lepton Lorentz factor from our simulations (results from the box-size scaling runs are not included). Filled and open symbols are used for simulations of reconnection in pair-proton and electron–proton plasmas, respectively.

$(\Theta_e \ll 1)$ with $\sigma \leqslant 10$ typically results in slopes and mean lepton energies that are not compatible with the FSRQ results.

BL Lac sources with $\langle\gamma_e\rangle \sim 10^2$–$10^3$ are compatible with our simulation results for reconnection in pair-proton plasmas with $\sigma \sim 3$–10, $\Theta_e \sim 10$, and $\kappa \sim 1$–10. The majority of BL Lac sources, however, require mean Lorentz factors $>10^3$. Reconnection in strongly magnetized plasmas ($\sigma > 10$) can lead to high values of the mean Lorentz factor, but concurrently produces hard power laws ($p < 2$) above the peak Lorentz factor γ_{inj} (e.g., orange curves) that do not agree with the fitting results for $\langle\gamma_e\rangle \gg 10^3$ (filled triangles). In this regime, however, we argue that γ_{inj} could be interpreted as the maximum Lorentz factor of a hard power law with $p < 2$, as found in our high-σ models, with p now corresponding to the index s_1 (see Equation (3)). Because the determination of the maximum Lorentz factor from the simulation spectra is not trivial (e.g., Werner et al. 2018), we refrain from drawing strong conclusions from the comparison of our results to the BL Lac sources in the sample of Celotti & Ghisellini (2008).

7.2. Equipartition Conditions

One factor that makes the principle of energy equipartition between particles and magnetic fields attractive is that it leads to minimum power solutions for blazar jets (e.g., Dermer et al. 2014; Petropoulou et al. 2016). The energy density ratio of radiating particles and magnetic fields in the blazar emitting region is usually a free parameter determined by the fitting of photon spectra. Leptonic emission models typically find $0.03 \lesssim u_{e^\pm}/u_B \lesssim 30$, although specific sources may require even higher values (e.g., Celotti & Ghisellini 2008; Tavecchio et al. 2010; Ghisellini et al. 2014). Alternatively, one can impose the constraint of rough energy equipartition between pairs and magnetic fields while searching for the best-fit model, as demonstrated successfully by Cerutti et al. (2014) and Dermer et al. (2014, 2015).

The post-reconnection ratio $u_{e^\pm}/u_B$ obtained from our simulations is plotted in Figure 14 as a function of the mean lepton Lorentz factor $\langle\gamma_e\rangle$. We find that $0.2 \lesssim u_{e^\pm}/u_B \lesssim 10$, with higher values obtained for hotter upstream plasmas. Even larger ratios, such as those inferred by modeling of TeV BL Lacs (e.g., Tavecchio et al. 2010), would require a pool of ultra-relativistically hot particles entering the reconnection region. The presence of a guide field (i.e., of a magnetic field component that does not reconnect) would make the reconnection region more magnetically dominated, thus leading to $u_{e^\pm}/u_B < 0.2$. More specifically, for electron–proton reconnection, it was demonstrated that the fraction of magnetic energy transferred to nonthermal electrons can decrease from ~50% (in the absence of guide field) to ~10% for a guide field with strength comparable to that of the reconnecting field component (Sironi et al. 2015; Werner & Uzdensky 2017). However, dissipation efficiencies as low as a few percent are still compatible with the global energetic requirements for AGN emission (Ghisellini et al. 2014; Sironi et al. 2015). A systematic study of the effects of the guide-field in pair-proton reconnection will be the topic of a future study.

8. Summary

For the first time, we have investigated magnetic reconnection in electron–positron–proton plasmas with a suite of large-scale 2D PIC simulations, covering a wide range of pair multiplicities ($\kappa = 1$–199) for different values of the all-species plasma magnetization ($\sigma = 1, 3$, and 10) and plasma temperature ($\Theta_e = 0.1, 1, 10$, and 100). In all cases we explored, protons in the upstream plasma have nonrelativistic temperatures and dominate the total mass.

The inflow rate of plasma into the reconnection region (i.e., the reconnection rate) ranges between $\sim 0.05 v_A$ and $0.15 v_A$ for a wide range of values of the hot pair plasma magnetization $\sigma_{e,h}$, with a weak trend toward higher rates for larger $\sigma_{e,h}$ values. The motion of the plasma outflow in the reconnection region, which is governed by the proton inertia, is relativistic with a maximum four-velocity that approaches the expected asymptotic value of $\sqrt{\sigma}$. We found no significant dependence of the outflow four-velocity on the pair multiplicity or temperature.

We showed that $\sim 1/3$ of the total energy remains in the post-reconnection magnetic field for $\sigma_{e,h} \gtrsim 3$, with the remaining 2/3 of the energy being shared between pairs and protons. Energy equipartition between protons and pairs is achieved for $\sigma \gg 1$ and $\sigma_{e,h} \gtrsim 30$. For $\sigma_{e,h} \lesssim 3$, most of the energy in the

reconnection region is carried by the pairs, with protons and magnetic fields contributing ∼1–10% to the total energy.

The reconnection process produces nonthermal particle energy distributions. We found that the mean Lorentz factor of the proton distribution (or more accurately, $\langle\gamma_i - 1\rangle$) is almost independent of the pair multiplicity and plasma temperature, but it is approximately equal to $\sigma/3$. The mean Lorentz factor of the pair distribution can be described by a simple analytical expression (see Equation (2)) for different values of $\sigma_{e,h}$, σ, and Θ_e.

The electron and positron energy distributions in the reconnection region are similar and can be modeled as a power law with slope p above a peak Lorentz factor—which, in most cases, is comparable with the mean Lorentz factor given by Equation (2). The energy distribution below the peak can, in general, be approximated by a flat power law (with index <0). We showed that p is mainly controlled by $\sigma_{e,h}$ (with harder power laws obtained for higher magnetizations) for a wide range of σ, Θ_e, and κ values. There is, however, a dependence of p on pair multiplicity, with power laws getting steeper as κ decreases from a few to unity.

We discussed the implications of our results in the context of AGN jets. We showed that reconnection in pair-proton plasmas naturally produces power-law pair distributions with slopes and average Lorentz factors similar to those obtained by leptonic modeling of the broadband jet emission. In general, we find that the majority of the modeling results can be explained in the context of reconnection in pair plasmas with multiplicities $\kappa \sim$ 1–20, magnetizations $\sigma \sim$ 1–10, and temperatures $\Theta_e \sim$ 1–10.

The authors thank the anonymous referee for a report that helped to improve the manuscript. M.P. acknowledges support from the Lyman Jr. Spitzer Postdoctoral Fellowship and the Fermi Guest Investigation grant 80NSSC18K1745. L.S. acknowledges support from DoE DE-SC0016542, NASA ATP NNX-17AG21G, NSF ACI-1657507, and NSF AST-1716567. A.S. is supported by NASA ATP 80NSSC18K1099 and the Simons Foundation (grant 267233). D.G. acknowledges support from NASA (grant ATP NNX17AG21G) and the NSF (grant AST-1816136). The simulations were performed using computational resources at the TIGRESS high-performance computer center at Princeton University, the Texas Advanced Computing Center (TACC) at The University of Texas at Austin (TG-AST180038, TG-AST180001), and at the NASA High-End Computing (HEC) Program through the NASA Advanced Supercomputing (NAS) Division at Ames Research Center.

Software: TRISTAN-MP (Buneman 1993; Spitkovsky 2005), IDL version 8.6 (Exelis Visual Information Solutions, Boulder, Colorado).

Appendix A
Parameter Definitions

We summarize the basic physical parameters that are relevant for this study (see Table 3) and provide their definitions below. The total (all-species) plasma magnetization is defined as

$$\sigma = \frac{B_0^2/4\pi}{n_i m_i c^2 + \frac{\hat{\gamma}_i}{\hat{\gamma}_i - 1} n_i k T_i + n_{e^\pm}\, m_e c^2 + \frac{\hat{\gamma}_e}{\hat{\gamma}_e - 1} n_{e^\pm}\, k T_e}, \quad (4)$$

where B_0 is the upstream magnetic field strength and n_i, $n_{e^\pm}$ are the number densities of protons and pairs, respectively, in the upstream region. Particles are initialized with temperatures $T_i = T_e$. The adiabatic indices for pairs and protons are computed iteratively using the equation of state by Synge (1957). We find that $\hat{\gamma}_e \approx 4/3$ $\hat{\gamma}_i \approx 5/3$, except for $\Theta_e = 0.1$, where $\hat{\gamma}_e \approx 1.5$. The cold plasma magnetization, which neglects the enthalpy terms, is defined by

$$\sigma_c = \frac{B_0^2}{4\pi (n_i m_i c^2 + n_{e^\pm}\, m_e c^2)}. \quad (5)$$

A key parameter in the study of the post-reconnection particle energy distributions (see Sections 5 and 6) is the hot pair plasma magnetization, which relates to the total σ as

$$\sigma_{e,h} = \sigma \frac{q\left(\frac{m_i}{m_e} + \frac{\hat{\gamma}_i \Theta_e}{\hat{\gamma}_i - 1}\right) + (2-q)\left(1 + \frac{\hat{\gamma}_e \Theta_e}{\hat{\gamma}_e - 1}\right)}{(2-q)\left(1 + \frac{\hat{\gamma}_e \Theta_e}{\hat{\gamma}_e - 1}\right)}. \quad (6)$$

The cold pair plasma magnetization is identical to $\sigma_{e,h}$ only for nonrelativistically hot plasmas ($\Theta_e \ll 1$), and is defined as

$$\sigma_{e,c} = \sigma \frac{q\left(\frac{m_i}{m_e} + \frac{\hat{\gamma}_i \Theta_e}{\hat{\gamma}_i - 1}\right) + (2-q)\left(1 + \frac{\hat{\gamma}_e \Theta_e}{\hat{\gamma}_e - 1}\right)}{2-q}. \quad (7)$$

Similar to the pair plasma, one can define the hot proton plasma magnetization:

$$\sigma_{i,h} = \sigma \frac{q\left(\frac{m_i}{m_e} + \frac{\hat{\gamma}_i \Theta_e}{\hat{\gamma}_i - 1}\right) + (2-q)\left(1 + \frac{\hat{\gamma}_e \Theta_e}{\hat{\gamma}_e - 1}\right)}{q\left(\frac{m_i}{m_e} + \frac{\hat{\gamma}_i \Theta_e}{\hat{\gamma}_i - 1}\right)}, \quad (8)$$

which is $\approx\sigma$ for all our cases. The cold proton plasma magnetization is written as

$$\sigma_{i,c} = \frac{\sigma m_e}{q m_i}\left[q\left(\frac{m_i}{m_e} + \frac{\hat{\gamma}_i \Theta_e}{\hat{\gamma}_i - 1}\right) + (2-q)\left(1 + \frac{\hat{\gamma}_e \Theta_e}{\hat{\gamma}_e - 1}\right)\right], \quad (9)$$

and it is the same as $\sigma_{i,h}$ as long as $\Theta_e \ll m_i/m_e$.

The ratio of the electron plasma pressure and the magnetic pressure (plasma β_e), which is a key parameter in studies of electron–proton reconnection, relates to $\sigma_{e,h}$ as

$$\beta_e \equiv \frac{8\pi n_{e^-} k T_e}{B_0^2} = \frac{2\Theta_e}{\sigma_{e,h}\,(2-q)\left(1 + \frac{\hat{\gamma}_e}{\hat{\gamma}_e - 1}\Theta_e\right)}. \quad (10)$$

If all particle species are relativistically hot ($\Theta_e \gg m_i/m_e$), then $\sigma_{e,h} \approx 2\sigma/(2-q)$ and β_e reaches its maximum value $\approx 1/4\sigma$.

Table 3
Descriptions, Symbols, and Definitions of Parameters Used in This Study

Parameter	Symbol	Definition
Pair Multiplicity	κ	$n_{e^\pm}/n_i$
Proton Fraction	q	$n_i/n_{e^-} = 2/(\kappa+1)$
Lepton Adiabatic Index	$\hat{\gamma}_e$	Synge (1957)
Proton Adiabatic Index	$\hat{\gamma}_i$	Synge (1957)
Total Plasma Magnetization	σ	Equation (4)
Hot Pair Plasma Magnetization	$\sigma_{e,h}$	Equation (1)
Cold Pair Plasma Magnetization	$\sigma_{e,c}$	Equation (7)
Hot Proton Plasma Magnetization	$\sigma_{i,h}$	Equation (8)
Cold Proton Plasma Magnetization	$\sigma_{i,c}$	Equation (9)
Electron Plasma β	β_e	Equation (10)
Plasma Electron Frequency	ω_{pe-}	Equation (12)
Plasma Proton Frequency	ω_{pi}	Equation (14)
Electron Larmor Radius	ρ_{Le}	Equation (15)
Proton Larmor Radius	ρ_{Li}	Equation (16)

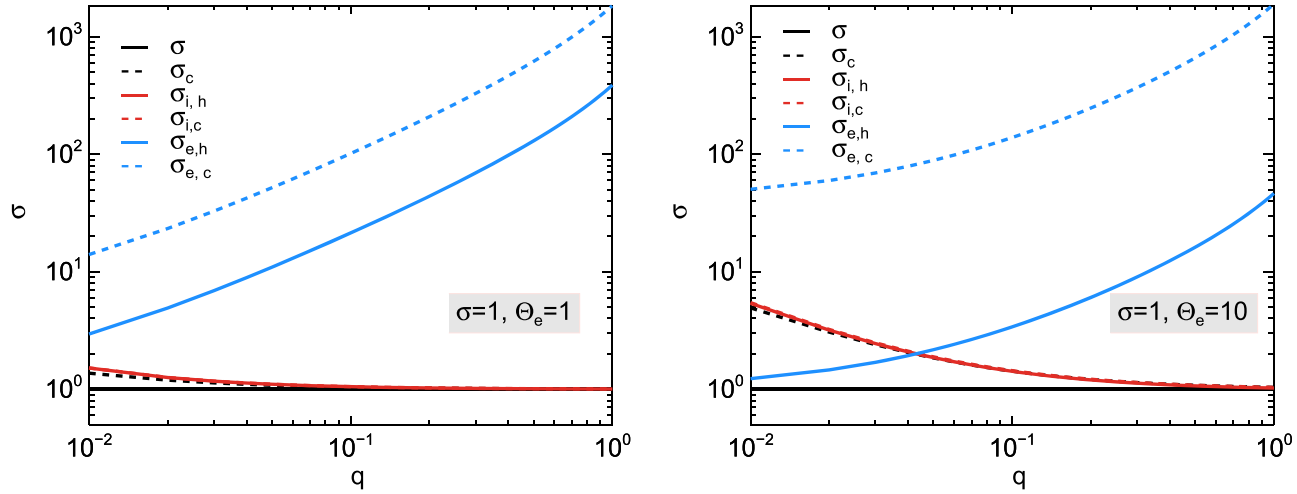

Figure 15. Various magnetizations—defined in Equations (4)–(9)—plotted as a function of the proton fraction q for $\sigma = 1$ and two plasma temperatures: $\Theta_e = 1$ (left panel) and $\Theta_e = 10$ (right panel).

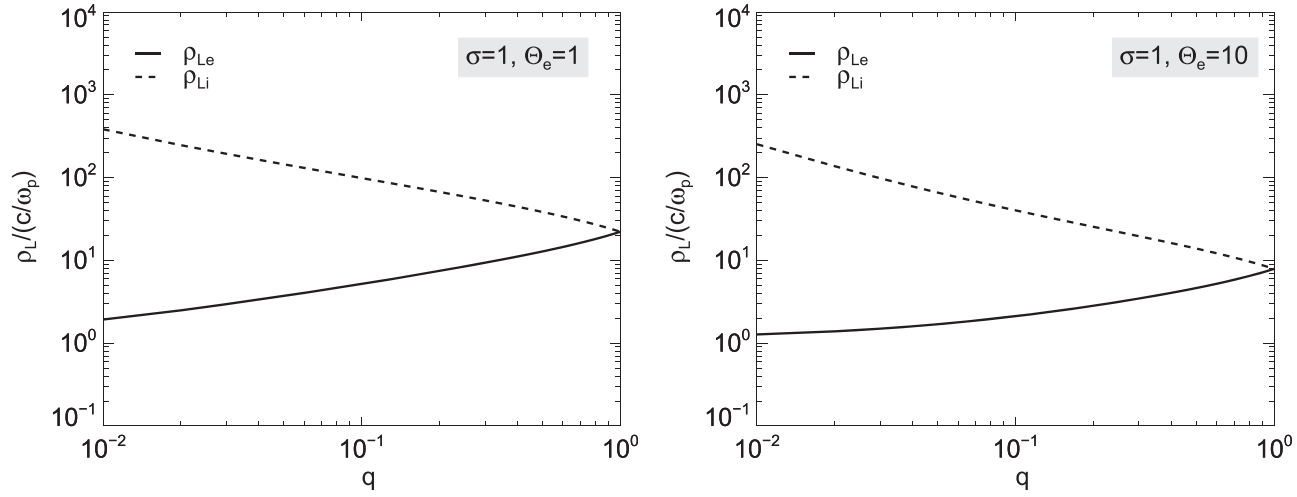

Figure 16. Electron and proton Larmor radii (see Equations (15) and (16), respectively) normalized to the all-species plasma skin depth plotted as a function of the proton fraction q for $\sigma = 1$ and two plasma temperatures: $\Theta_e = 1$ (left panel) and $\Theta_e = 10$ (right panel).

Let ω_p denote the all-species plasma frequency:

$$\omega_p^2 = \omega_{pe^-}^2 + \omega_{pe^+}^2 + \omega_{pi}^2 \tag{11}$$

where the electron, positron, and proton plasma frequencies are given by

$$\omega_{pe^-}^2 = \frac{4\pi n_{e^-} e^2}{m_e\left(1 + \frac{\Theta_e}{\hat{\gamma}_e - 1}\right)}, \tag{12}$$

$$\omega_{pe^+}^2 = \omega_{pe^-}^2 (1 - q), \tag{13}$$

and

$$\omega_{pi}^2 = \omega_{pe^-}^2 \frac{m_e}{m_i} q \frac{1 + \frac{\Theta_e}{\hat{\gamma}_e - 1}}{1 + \frac{\Theta_i}{\hat{\gamma}_i - 1}}. \tag{14}$$

Finally, we define the Larmor radius of electrons and protons with Lorentz factors $\sigma_{e,c}$ and $\sigma_{i,c}$, respectively, assuming that all the magnetic energy is transferred to the particles:

$$\rho_{Le} \equiv \frac{\sigma_{e,c}\, m_e c^2}{eB_0} = \frac{c}{\omega_{pe^-}}\left(\frac{\sigma_{e,c}}{2 - q}\right)^{1/2}\left(1 + \frac{\Theta_e}{\hat{\gamma}_e - 1}\right)^{-1/2} \tag{15}$$

and

$$\rho_{Li} \equiv \frac{\sigma_{i,c}\, m_i c^2}{eB_0} = \frac{c}{\omega_{pe^-}}\left(\frac{\sigma_{i,c}}{q}\frac{m_i}{m_e}\right)^{1/2}\left(1 + \frac{\Theta_e}{\hat{\gamma}_e - 1}\right)^{-1/2}. \tag{16}$$

Figures 15 and 16 show the various magnetizations and particle Larmor radii as a function of the proton fraction q, which is related to the pair multiplicity κ as $q = 2/(\kappa + 1)$.

Appendix B
Appearance of the Reconnection Layer

In Section 3.2, we explored the effects of the pair multiplicity on the appearance of the layer. More specifically, we showed that the layer becomes more structured (i.e., more secondary plasmoids) as the pair multiplicity decreases, with other parameters kept the same. One could argue that these differences are merely a result of the different box sizes in terms of the proton skin depth. A straightforward way of checking this possibility is to compare cases with different physical conditions, but similar box sizes in terms of ρ_{Li}.

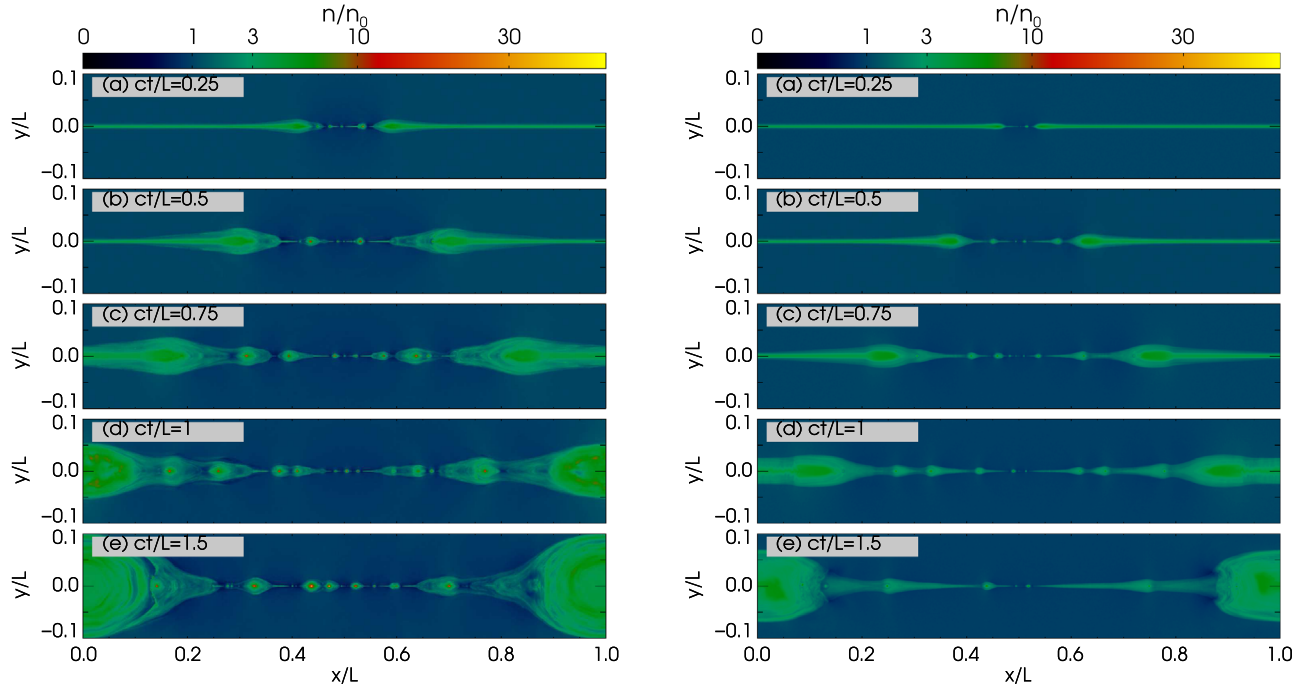

Figure 17. Snapshots of the 2D structure of the all-species particle number density n (normalized to the number density n_0 far from the reconnection layer) from two simulations with different physical conditions but similar box size in terms of ρ_{Li} (see runs A2 and B1 in Table 1): $\sigma = 1$, $\Theta_e = 1$, $\kappa = 19$, $L/\rho_{Li} \simeq 53$ (left); and $\sigma = 1$, $\Theta_e = 10$, $\kappa = 66$, $L/\rho_{Li} \simeq 53$ (right).

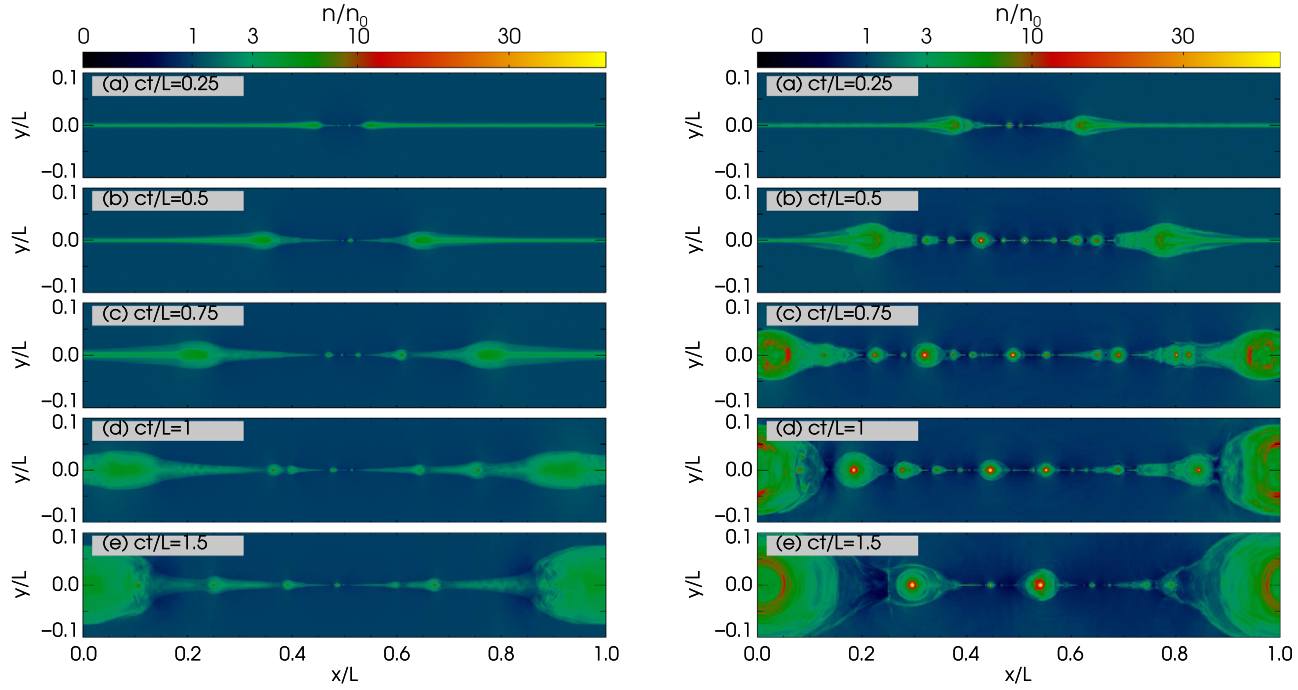

Figure 18. Same as in Figure 17, but for: $\sigma = 1$, $\Theta_e = 10$, $\kappa = 19$, $L/\rho_{Li} \simeq 130$ (left); and $\sigma = 3$, $\Theta_e = 1$, $\kappa = 6$, $L/\rho_{Li} \simeq 122$ (right).

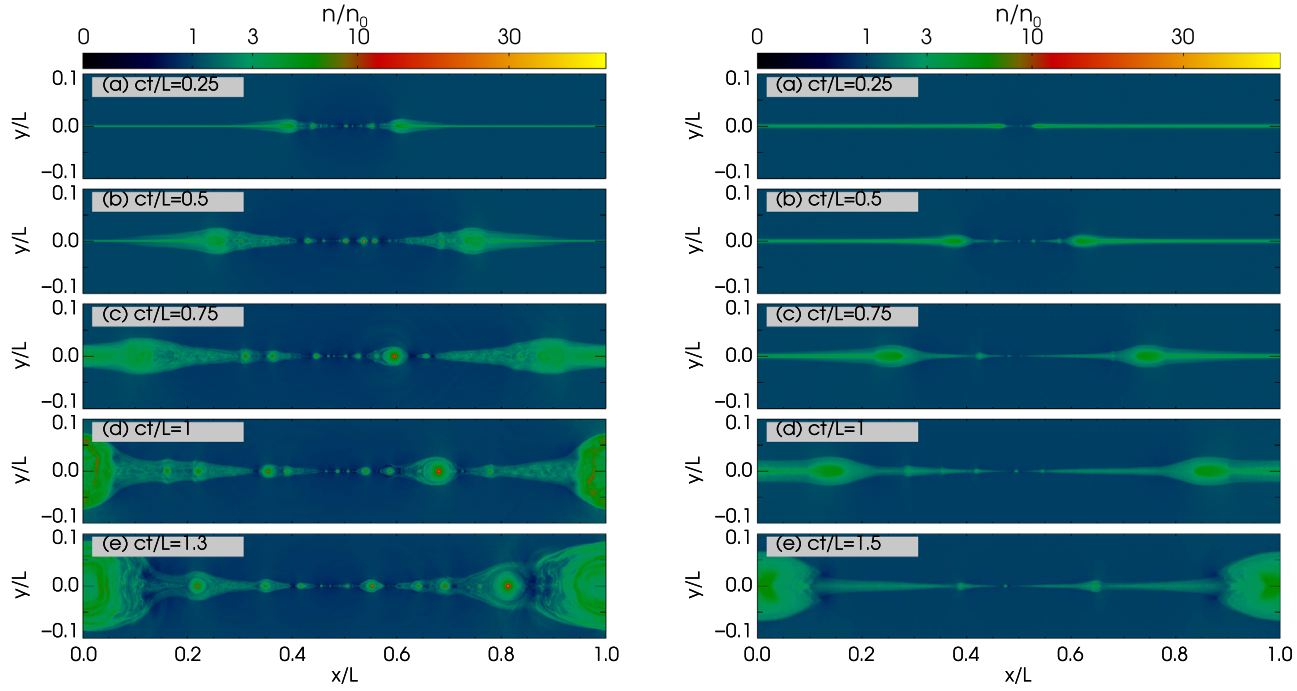

Figure 19. Same as in Figure 17, but for: $\sigma = 1$, $\Theta_e = 1$, $\kappa = 6$, $L/\rho_{Li} \simeq 211$ (left); and $\sigma = 1$, $\Theta_e = 100$, $\kappa = 19$, $L/\rho_{Li} \simeq 206$ (right).

Snapshots of the density structure from three such pairs of simulations are presented in Figures 17–19. These comparative plots clearly show that the appearance of the layer is significantly affected by the plasma conditions.

Appendix C
Effects of Box Size

We discuss the effect of the box size on the inflow and outflow rates as well as on the post-reconnection particle energy distributions.

We selected two simulations (see runs A3–A5, C4–C5 in Table 1) and varied the box size in the x-direction, as indicated in Figure 20. Although the peak inflow rate is systematically higher for smaller box sizes, the difference is less than ∼3–5%. The temporal evolution of the reconnection rate is similar for all box sizes (top panel in Figure 20), until the formation of the boundary island inhibits the inflow of plasma in the reconnection region, as shown in the bottom panel (blue line). The asymptotic outflow four-velocity is independent of the box size, even for layer lengths of only a few hundred ρ_{Le}.

Snapshots of the post-reconnection particle energy distributions from simulations with different box sizes are shown in Figure 21. The power-law segment of the pair energy spectra is similar for the different cases, suggesting a saturation of the power-law slope already for boxes as small as $L \sim 300\,\rho_{Le}$ (see also Ball et al. 2018). Thus, we are confident that the power-law slopes we report in Section 6.3 (Figure 12), which were obtained for the spectra plotted with blue lines in Figure 21, are robust. The high-energy cutoff of the pair distribution, however, increases (almost linearly) with increasing box size, as shown more clearly in the right plot of Figure 21. Even larger domains are needed for capturing the asymptotic temporal evolution of the cutoff energy. The proton distribution depends strongly on the box size, for both σ values we considered. A well-developed power-law forms above the peak proton energy in the largest simulations, thus supporting the argument that reconnection results in extended nonthermal proton distributions (see also Section 6.3).

The effects of the box size on the quantities discussed above and in Section 5 are summarized in Figure 22. The outflow four-velocities are not included in this plot, because they are almost the same for the box sizes we considered.

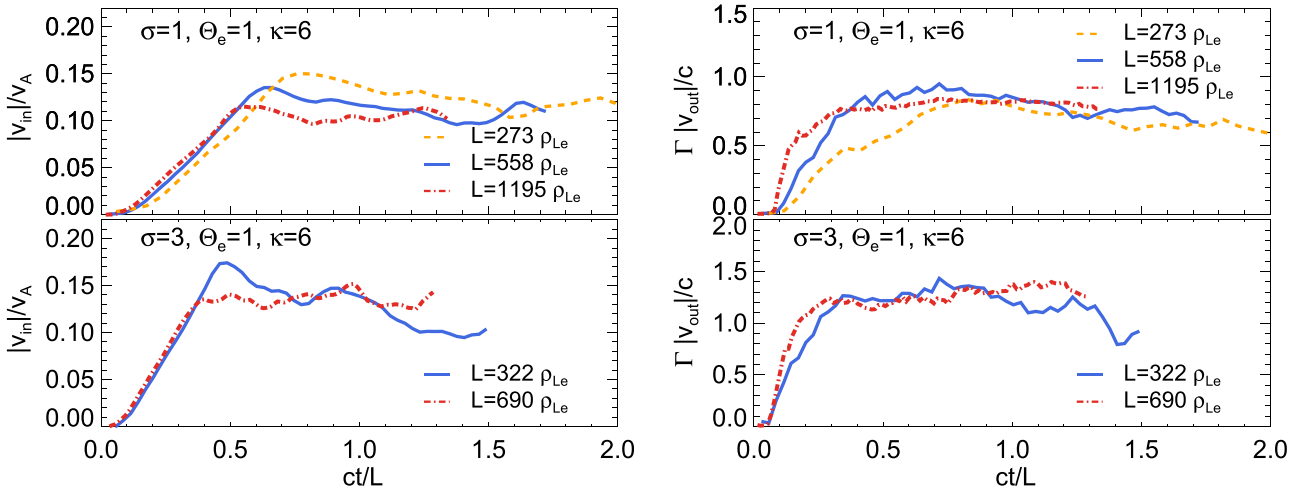

Figure 20. Temporal evolution of the inflow speed (left panel) and the outflow four-velocity (right panel) from simulations of reconnection in plasmas with: $\sigma = 1$, $\Theta_e = 1$, $\kappa = 6$ (top panels); and $\sigma = 3$, $\Theta_e = 1$, $\kappa = 6$ (bottom panels) for different box sizes marked on the plot (see runs A3–A5, C4–C5 in Table 1).

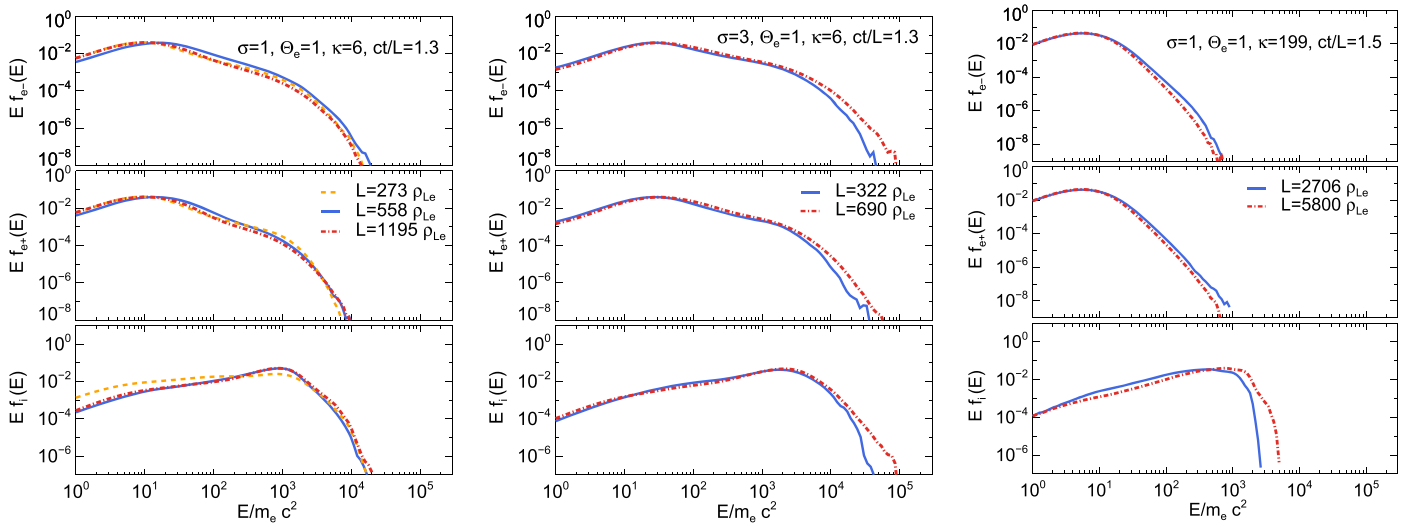

Figure 21. Post-reconnection electron, positron, and proton energy distributions computed from simulations of reconnection in plasmas with: $\sigma = 1$, $\Theta_e = 1$, $\kappa = 6$ (left panel); $\sigma = 3$, $\Theta_e = 1$, $\kappa = 6$ (middle panel); and $\sigma = 1$, $\Theta_e = 1$, $\kappa = 199$ (right panel), for different box sizes marked on the plot (see runs A3–A5, C4–C5, A0 and A9 in Table 1). The spectra are computed at the same time (in units of L/c) and are normalized to the total number of protons within the reconnection region at that time.

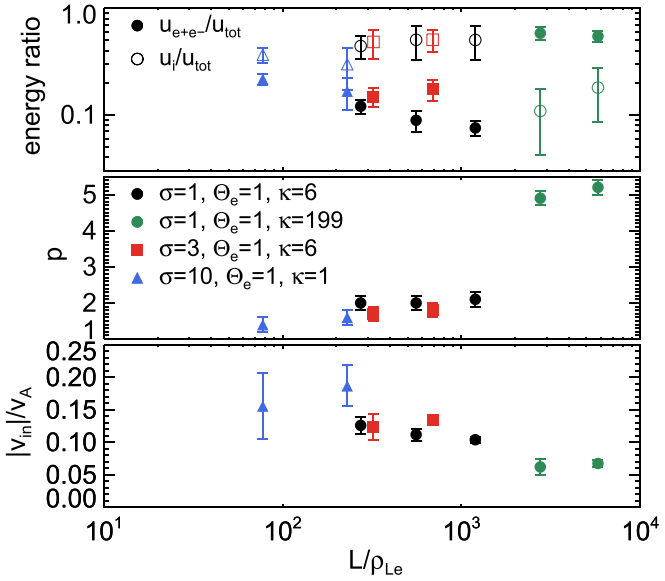

Figure 22. Summary plot showing the dependence of various quantities on the size of the simulation box. From top to bottom: energy ratios for pairs (filled symbols) and protons (open symbols), power-law slope of the lepton energy spectrum (as computed at the end of each simulation), and time-averaged reconnection rate. Error bars in the top and bottom panels indicate the standard deviation during the course of the simulation. A systematic error of ±0.2 is assigned in all power-law slopes (middle panel).

Appendix D
Dependence of the Mean Lepton Lorentz Factor on Physical Parameters

The mean energy of the relativistic pair distribution is of astrophysical importance, as it can be imprinted on the radiated nonthermal photon spectra (for details, see Section 7). We therefore attempted to quantify the dependence of mean lepton Lorentz factor on the physical parameters (σ, Θ_e, and κ) using a proxy of $\langle\gamma_e - 1\rangle$, as defined in Section 5. We caution the reader that the latter does not necessarily refer to a pure power-law energy distribution. In fact, the definition of $\langle\gamma_e - 1\rangle$ is agnostic to the shape of the lepton energy distribution.

In general, we find that $\langle\gamma_e - 1\rangle$ can be described by

$$\langle\gamma_e - 1\rangle = a(\sigma, \Theta)\kappa^{-\chi(\sigma,\Theta)} + b(\sigma, \Theta), \quad (17)$$

where a, b, and χ are obtained from a χ^2 fit to the data. The best-fit values and the associated 1σ statistical errors are summarized in Table 4. We note that cases with $\sigma = 1$, $\Theta_e = 0.1$; $\sigma = 10$, $\Theta_e = 1$; and $\sigma = 10$, $\Theta_e = 10$ are excluded from the fit, because the number of κ values is the same or less than the free parameters of Equation (17). Nevertheless, we still find that $\langle\gamma_e - 1\rangle \propto \kappa^{-1}$.

Table 4
Results of a χ^2 Fit to Equation (17)

σ	Θ_e	a	χ	b
1	1	114.9 ± 18.1	1.5 ± 0.2	6.5 ± 0.7
1	10	149.7 ± 17.6	1.3 ± 0.2	46.8 ± 2.2
1	100	328.9 ± 7.1	1.6 ± 0.1	456.7 ± 3.4
3	1	565.7 ± 73.6	1.1 ± 0.1	13.5 ± 2.1
3	10	603.7 ± 36.7	1.2 ± 0.1	85.7 ± 7.0

Note. We exclude cases with less data points than the number of free model parameters. The 1σ statistical errors are also listed in the table.

Appendix E
Effects of Plasma Temperature on Pair Energy Spectra

The post-reconnection particle energy distributions obtained for the highest-temperature simulations (H1–H3 in Table 1) show a high-energy component that forms at late times, as illustrated in Figure 23 (left panel). This can be described by a power law with slope $p \sim 3.2$–3.6 (see Table 2), which is harder than the power laws obtained for lower temperatures but similar $\sigma_{e,h}$ values (see Figure 12).

Snapshots of the pair energy distributions from simulations with the same magnetization and multiplicity, but different plasma temperatures, are shown in the middle and right panels of Figure 23. Although $\Theta_e = 100$ shows a prominent high-energy component in the distributions that is independent of κ, we see a hint of this component at lower temperatures ($\Theta_e = 10$) only at $\kappa = 199$ (right panel). These results imply that the high-energy component of the spectrum is not just related to the plasma temperature. In all the cases that show a high-energy component, the common denominator is the high β_e (i.e., $\beta_e > 0.1$; see Table 2).

Similar results have been reported by Ball et al. (2018) for transrelativistic reconnection in electron–proton plasmas with high β_e approaching the maximum value $1/4\sigma$ (when both electrons and protons start as relativistically hot). The formation of the high-energy component was attributed to a Fermi-like acceleration of particles with initial energy $\sim kT_e$ bouncing between the reconnection outflow and the stationary boundary island (see Section 6.3 in Ball et al. 2018). The fact that it takes some time for the boundary island to grow is in agreement with the late-time formation of the high-energy component in the spectrum.

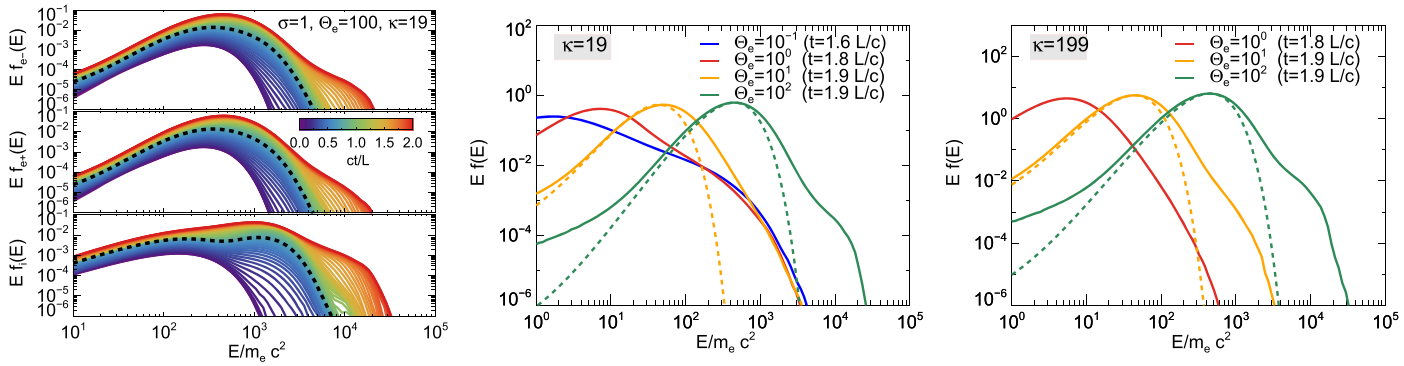

Figure 23. Left panel: same as in Figure 9, but for $\Theta_e = 100$, $\sigma = 1$, and $\kappa = 19$. Middle panel: electron energy distributions from the post-reconnection region (solid lines) for simulations with $\sigma = 1$, $\kappa = 19$, and different temperatures marked on the plot. All spectra are computed at the end of each simulation (see inset legend) and are normalized to the total number of protons within the reconnection region at that time. A relativistic Maxwell–Jüttner distribution with temperature $1.5\Theta_e$ (normalized to match the maximum value of the respective electron energy distribution) is also plotted for comparison for $\Theta_e = 10$ and 100 (dashed lines). Right panel: same as in the middle panel, but for $\kappa = 199$.

ORCID iDs

Maria Petropoulou https://orcid.org/0000-0001-6640-0179

References

Ahnen, M. L., Ansoldi, S., Antonelli, L. A., et al. 2018, A&A, 620, A181
Aleksić, J., Alvarez, E. A., Antonelli, L. A., et al. 2012, ApJ, 748, 46
Ball, D., Sironi, L., & Özel, F. 2018, ApJ, 862, 80
Beniamini, P., & Giannios, D. 2017, MNRAS, 468, 3202
Buneman, O. 1993, Computer Space Plasma Physics (Tokyo: Terra Scientific), 67
Celotti, A., & Ghisellini, G. 2008, MNRAS, 385, 283
Cerruti, M., Boisson, C., & Zech, A. 2013, A&A, 558, A47
Cerutti, B., Werner, G. R., Uzdensky, D. A., & Begelman, M. C. 2012, ApJL, 754, L33
Cerutti, B., Werner, G. R., Uzdensky, D. A., & Begelman, M. C. 2014, ApJ, 782, 104
Christie, I. M., Petropoulou, M., Sironi, L., & Giannios, D. 2019, MNRAS, 482, 65
Costamante, L., Ghisellini, G., Giommi, P., et al. 2001, A&A, 371, 512
Daughton, W., & Karimabadi, H. 2007, PhPl, 14, 072303
Daughton, W., Nakamura, T. K. M., Karimabadi, H., Roytershteyn, V., & Loring, B. 2014, PhPl, 21, 052307
Dermer, C. D., Cerruti, M., Lott, B., Boisson, C., & Zech, A. 2014, ApJ, 782, 82
Dermer, C. D., Yan, D., Zhang, L., Finke, J. D., & Lott, B. 2015, ApJ, 809, 174
Drenkhahn, G., & Spruit, H. C. 2002, A&A, 391, 1141
Fossati, G., Maraschi, L., Celotti, A., Comastri, A., & Ghisellini, G. 1998, MNRAS, 299, 433
Ghisellini, G. 2012, MNRAS, 424, L26
Ghisellini, G., Ghirlanda, G., Nava, L., & Celotti, A. 2010, MNRAS, 403, 926
Ghisellini, G., Tavecchio, F., Maraschi, L., Celotti, A., & Sbarrato, T. 2014, Natur, 515, 376
Giannios, D. 2008, A&A, 480, 305
Giannios, D. 2013, MNRAS, 431, 355
Giannios, D., Uzdensky, D. A., & Begelman, M. C. 2009, MNRAS, 395, L29
Giannios, D., Uzdensky, D. A., & Begelman, M. C. 2010, MNRAS, 402, 1649
Guo, F., Li, H., Daughton, W., Li, X., & Liu, Y.-H. 2016, PhPl, 23, 055708
Guo, F., Li, H., Daughton, W., & Liu, Y.-H. 2014, PhRvL, 113, 155005
Guo, F., Liu, Y.-H., Daughton, W., & Li, H. 2015, ApJ, 806, 167
Hakobyan, H., Philippov, A., & Spitkovsky, A. 2019, ApJ, 877, 53
Kagan, D., Milosavljević, M., & Spitkovsky, A. 2013, ApJ, 774, 41
Kagan, D., Nakar, E., & Piran, T. 2018, MNRAS, 476, 3902
Kammoun, E. S., Nardini, E., Risaliti, G., et al. 2018, MNRAS, 473, L89
Liu, W., Li, H., Yin, L., et al. 2011, PhPl, 18, 052105
Liu, Y.-H., Guo, F., Daughton, W., Li, H., & Hesse, M. 2015, PhRvL, 114, 095002
Lyubarsky, Y., & Kirk, J. G. 2001, ApJ, 547, 437
Lyubarsky, Y. E. 2005, MNRAS, 358, 113
Lyutikov, M., & Blandford, R. 2003, arXiv:astro-ph/0312347
Madejski, G. M., Nalewajko, K., Madsen, K. K., et al. 2016, ApJ, 831, 142
Melzani, M., Walder, R., Folini, D., Winisdoerffer, C., & Favre, J. M. 2014, A&A, 570, A112
Nalewajko, K., Uzdensky, D. A., Cerutti, B., Werner, G. R., & Begelman, M. C. 2015, ApJ, 815, 101
Nalewajko, K., Yuan, Y., & Chruślińska, M. 2018, JPlPh, 84, 755840301
Parfrey, K., Philippov, A., & Cerutti, B. 2019, PhRvL, 122, 035101
Pétri, J., & Lyubarsky, Y. 2007, A&A, 473, 683
Petropoulou, M., Giannios, D., & Sironi, L. 2016, MNRAS, 462, 3325
Petropoulou, M., & Sironi, L. 2018, MNRAS, 481, 5687
Philippov, A. A., & Spitkovsky, A. 2014, ApJL, 785, L33
Romanova, M. M., & Lovelace, R. V. E. 1992, A&A, 262, 26
Rowan, M. E., Sironi, L., & Narayan, R. 2017, ApJ, 850, 29
Sikora, M., & Madejski, G. 2000, ApJ, 534, 109
Sikora, M., Madejski, G., Moderski, R., & Poutanen, J. 1997, ApJ, 484, 108
Sironi, L., & Cerutti, B. 2017, in Modelling Pulsar Wind Nebulae, ed. D. F. Torres (Cham: Springer), 247
Sironi, L., Giannios, D., & Petropoulou, M. 2016, MNRAS, 462, 48
Sironi, L., Petropoulou, M., & Giannios, D. 2015, MNRAS, 450, 183
Sironi, L., & Spitkovsky, A. 2011a, ApJ, 741, 39
Sironi, L., & Spitkovsky, A. 2011b, ApJ, 726, 75
Sironi, L., & Spitkovsky, A. 2012, CS&D, 5, 014014
Sironi, L., & Spitkovsky, A. 2014, ApJL, 783, L21
Spitkovsky, A. 2005, in AIP Conf. Ser. 801, Astrophysical Sources of High Energy Particles and Radiation, ed. T. Bulik, B. Rudak, & G. Madejski (Melville, NY: AIP), 345
Spruit, H. C., Daigne, F., & Drenkhahn, G. 2001, A&A, 369, 694
Synge, J. L. 1957, The Relativistic Gas (Amsterdam: North-Holland), 33
Tavecchio, F., Ghisellini, G., Ghirlanda, G., Foschini, L., & Maraschi, L. 2010, MNRAS, 401, 1570
Thompson, C. 1994, MNRAS, 270, 480
Ulrich, M.-H., Maraschi, L., & Urry, C. M. 1997, ARA&A, 35, 445
Usov, V. V. 1994, MNRAS, 267, 1035
Werner, G. R., & Uzdensky, D. A. 2017, ApJL, 843, L27
Werner, G. R., Uzdensky, D. A., Begelman, M. C., Cerutti, B., & Nalewajko, K. 2018, MNRAS, 473, 4840
Werner, G. R., Uzdensky, D. A., Cerutti, B., Nalewajko, K., & Begelman, M. C. 2016, ApJL, 816, L8
Zenitani, S., & Hoshino, M. 2001, ApJL, 562, L63
Zenitani, S., & Hoshino, M. 2005, PhRvL, 95, 095001
Zenitani, S., & Hoshino, M. 2007, ApJ, 670, 702
Zenitani, S., & Hoshino, M. 2008, ApJ, 677, 530